



NGC 628 in SIGNALS: Explaining the Abundance-ionization Correlation in H II Regions

Ray Garner, III^{1,2}, Robert Kennicutt, Jr.^{1,2,3}, Laurie Rousseau-Nepton^{4,5,6}, Grace M. Olivier^{1,2}, David Fernández-Arenas⁶, Carmelle Robert^{7,8}, René Pierre Martin⁹, and Philippe Amram¹⁰

¹ Department of Physics and Astronomy, Texas A&M University, 578 University Drive, College Station, TX 77843, USA; ray.three.garner@gmail.com
² George P. and Cynthia W. Mitchell Institute for Fundamental Physics & Astronomy, Texas A&M University, 578 University Drive, College Station, TX 77843, USA

³ Department of Astronomy and Steward Observatory, University of Arizona, 933 N. Cherry Avenue, Tucson, AZ 85721, USA

⁴ Dunlap Institute of Astronomy and Astrophysics, University of Toronto, 50 St. George Street, Toronto, ON, M5S 3H4, Canada

⁵ Department of Astronomy & Astrophysics, University of Toronto, 50 St. George Street, Toronto, ON, M5S 3H4, Canada

⁶ Canada-France-Hawaii Telescope, 65-1238 Mamalahoa Highway, Kamuela, HI 96743, USA

⁷ Département de physique, de génie physique et d'optique, Université Laval, Québec City, QC G1V 0A6, Canada

⁸ Centre de recherche en astrophysique du Québec, Université de Montréal, Montréal, QC H3C 3J7, Canada

⁹ Department of Physics and Astronomy, University of Hawaii at Hilo, Hilo, HI 96720, USA

¹⁰ Aix Marseille University, CNRS, CNES, Laboratoire d'astrophysique de Marseille, 38 Rue Frédéric Joliot Curie, Marseille 13013, France

Received 2024 October 09; revised 2024 November 20; accepted 2024 November 24; published 2024 December 26

Abstract

The variations of oxygen abundance and ionization parameter in H II regions are usually thought to be the dominant factors that produced variations seen in observed emission-line spectra. However, if and how these two quantities are physically related is hotly debated in the literature. Using emission line data of NGC 628 observed with SITELLE as part of the Star formation, Ionized Gas, and Nebular Abundances Legacy Survey (SIGNALS), we use a suite of photoionization models to constrain the abundance and ionization parameters for over 1500 H II regions throughout its disk. We measure an anticorrelation between these two properties, consistent with expectations, although with considerable scatter. Secondary trends with dust extinction and star formation rate surface density potentially explain the large scatter observed. We raise concerns throughout regarding various modeling assumptions and their impact on the observed correlations presented in the literature.

Unified Astronomy Thesaurus concepts: Galaxy chemical evolution (580); Photoionization (2060); Interstellar medium (847); H II regions (694)

1. Introduction

Classical H II regions are large, low-density clouds of partially ionized gas in which star formation has recently taken place. These clouds are ionized by the hot, massive, short-lived stars that emit large amounts of ultraviolet radiation. Despite coming in a wide range of sizes and morphologies, each with its own ionizing populations, one can learn about their chemical compositions and their ionization states by studying their emission-line spectra.

Numerous prescriptions exist in the literature to estimate the metallicity of an H II region.¹¹ The most direct and physically motivated method is to measure the electron temperature, T_e , of the ionized gas using the intensity of one or more temperature-sensitive auroral lines like [O III] $\lambda\lambda 496, 500, 501$. Unfortunately, these auroral lines are intrinsically faint and not often observed. This is a common issue, so “strong-line” calibrations have been presented that use easily measurable strong lines to estimate the oxygen abundance (see M. Peimbert et al. 2017; E. Pérez-Montero 2017; R. Maiolino & F. Mannucci 2019 for excellent reviews).

While these strong-line calibrations are considered ubiquitously in the literature, there are still unsolved issues and

secondary dependencies remaining. One such dependency is the ionization parameter, \mathcal{U} , defined as the ratio of the number density of incident ionizing photons and the number density of hydrogen atoms (L. J. Kewley & M. A. Dopita 2002). Thus, the ionization parameter gives an insight into the efficiency of the radiation that ionizes the gas, where the higher the value, the more easily the radiation can ionize metals. Unfortunately, this parameter is almost impossible to be measured directly and depends on the internal structure of an H II region. Additionally, those strong-line calibrations derived from photoionization models strongly depend on the input parameters, which are often hard to constrain (e.g., metal depletion, density distribution, and geometry). This might lead to the discrepancy in abundance calibrations where empirical and theoretical calibrations disagree by up to 0.5 dex (e.g., L. J. Kewley & S. L. Ellison 2008; J. Moustakas et al. 2010). A similar, yet unexplored, situation exists in the calibrations for the ionization parameter, where they differ by an order of magnitude (K. Kreckel et al. 2019; M. Mingozi et al. 2020). Thus, calibrations derived entirely from photoionization models are not to be trusted implicitly and require deeper insight into their effect on observed correlations.

One such correlation potentially impacted by photoionization modeling is between metallicity and the ionization parameter. These are often assumed to be the main contributors to the variations of line ratios among star-forming regions. Early works found an anticorrelation between these two quantities (M. A. Dopita & I. N. Evans 1986; F. Bresolin et al. 1999; M. A. Dopita et al. 2006; C. Maier et al. 2006; T. Nagao et al. 2006). M. A. Dopita et al. (2006) presented a

¹¹ In this paper, “metallicity” and “oxygen abundance” will be used interchangeably unless otherwise noted.



Original content from this work may be used under the terms of the [Creative Commons Attribution 4.0 licence](#). Any further distribution of this work must maintain attribution to the author(s) and the title of the work, journal citation and DOI.

theoretical explanation using a wind-driven bubble model for H II regions where two effects might take place at higher metallicities: (1) stellar winds become more opaque and absorb ionizing photons, reducing the ionization parameter, and (2) the stellar atmospheres scatter photons more effectively, leading to stronger winds, enlarging the H II region and diluting the ionizing flux (see also M. Cantiello et al. 2007; J. J. Eldridge et al. 2011; L. Xiao et al. 2018). Other effects might also be present, including dust absorption producing a softer radiation field (M. A. Dopita & I. N. Evans 1986; S. C. C. Yeh & C. D. Matzner 2012; A. A. Ali 2021), a correlation between the initial mass function (IMF) and metallicity (I. Martín-Navarro et al. 2015), or a correlation between ionization and age (E. W. Pellegrini et al. 2020; F. Scheuermann et al. 2023). Regardless of the cause, other studies have since observationally supported the existence of this anticorrelation (e.g., E. Pérez-Montero 2014; C. Morisset et al. 2016; C. Espinosa-Ponce et al. 2022).

Interestingly, many studies do not find an anticorrelation between metallicity and the ionization parameter, instead finding either no correlation or a positive correlation (e.g., R. C. Kennicutt & D. R. Garnett 1996; D. R. Garnett et al. 1997; O. L. Dors et al. 2011; M. A. Dopita et al. 2014; H. Poetrodjojo et al. 2018; K. Kreckel et al. 2019; M. Mingozi et al. 2020; K. Grasha et al. 2022; X. Ji & R. Yan 2022). A search began to find a secondary parameter to explain these positive correlations, or the scatter observed in the anticorrelations. For example, M. A. Dopita et al. (2014) found a positive correlation between \mathcal{U} and the star formation rate (SFR) in luminous infrared galaxies, where a higher SFR could increase \mathcal{U} either due to the higher mass of the ionizing star cluster or a change in the geometry of the cloud. Meanwhile, E. W. Pellegrini et al. (2020) and M. Mingozi et al. (2020) found a correlation not between \mathcal{U} and SFR but between \mathcal{U} and specific star formation rate (sSFR) as traced by the H α equivalent width. These studies proposed that these relations hold for all galaxies, although other studies have found that the relations are different for individual galaxies (H. Poetrodjojo et al. 2018).

In this work, we attempt to unravel some of these dependencies by using emission-line fluxes from H II regions in the nearby spiral galaxy NGC 628 collected with the Spectro-Imageur à Transformée de Fourier pour l’Étude en Long et en Large des raies d’Émission (SITELLE; L. Drissen et al. 2019) as part of the Star formation, Ionized Gas, and Nebular Abundances Legacy Survey (SIGNALS; L. Rousseau-Nepton et al. 2019). NGC 628 is a well-known spiral galaxy seen almost face-on. Its relatively close distance ($D = 9.0$ Mpc; G. Dhungana et al. 2016) enables its properties to be studied in detail. Notably, given its close distance and subsequently high spatial resolution (~ 35 pc with SITELLE; L. Rousseau-Nepton et al. 2018), even the faintest low-luminosity H II regions can be resolved. Thus, we are in a key position to explore the potential correlation between metallicity and ionization parameter in NGC 628.

While the correlations and anticorrelations found rely on a deep understanding of the physical conditions of H II regions, the uncertainties of photoionization modeling (X. Ji & R. Yan 2022) and the resolved scale of observations (L. J. Kewley et al. 2019) still need to be understood. Since we are studying the H II regions of a singular galaxy, we have the ability to tailor photoionization models to our data set and

estimate abundances and ionization parameters in a self-consistent Bayesian framework (e.g., A. D. Thomas et al. 2018). This allows for complete freedom in the assumptions and priors used rather than relying on literature calibrations. Our high spatial resolution also gives us unprecedented insight into the role this plays in measuring an (anti)correlation between these two properties.

This paper is organized as follows. Section 2 describes the observational data and our H II region catalog. In Section 3, we motivate our use of custom photoionization models by exploring the discrepancies between existing ionization parameter calibrations. We describe our CLOUDY photoionization models and estimate parameters from these models using NebulaBayes in Section 4. Given this relatively new technique, we justify its use by recovering numerous gradients and trends already discovered in NGC 628 in Section 5. Section 6 presents the anticorrelation between metallicity and the ionization parameter in NGC 628, and discusses possible secondary parameters causing the large amount of scatter we measure. Finally, we present our conclusions in Section 7.

Throughout this work, we use the following abbreviations for some of the frequently mentioned emission lines. We denote [N II] $\lambda\lambda 6583$, [S II] $\lambda\lambda 6717, 6731$, [S III] $\lambda\lambda 9069, 9531$, [O III] $\lambda\lambda 5007, 4959$, and [O II] $\lambda 3727$ as [N II], [S II], [S III], [O III], and [O II], respectively, unless otherwise noted.

2. Data Reduction and H II Region Selection

The data for NGC 628 were taken over two observing sessions using the imaging Fourier transform spectrograph SITELLE at the Canada–France–Hawaii Telescope (CFHT) as part of SIGNALS (L. Rousseau-Nepton et al. 2019). Full details of our observation and reduction techniques are given in L. Rousseau-Nepton et al. (2018). Table 1 of the aforementioned paper gives quantitative information about the filters and total exposure times for our data. Briefly, we summarize our observations here.

SITELLE is a Michelson interferometer inserted into the collimated beam of an astronomical camera system (L. Drissen et al. 2019). Its large field of view (FOV: $11' \times 11'$) with complete spatial coverage, a high spectral resolution of up to $R \simeq 10,000$, and a broad wavelength range from 3500 – 9000 Å with excellent efficiency in the blue part of the spectrum make this an ideal instrument to study the H II regions of any local galaxy. Filters are necessary with SITELLE to reduce the noise in a selected bandpass. For this project, three filters were used, namely SN1 (3640–3850 Å), SN2 (4840–5120 Å), and SN3 (6480–6860 Å). These filters allow for the measurement of multiple strong emission lines: [O II] $\lambda 3727$, H β , [O III] $\lambda\lambda 4959, 5007$, [N II] $\lambda\lambda 6548, 6583$, H α , He I $\lambda 6678$, and [S II] $\lambda\lambda 6717, 6731$. The right panel of Figure 1 shows the deep image produced by adding, for each pixel, the whole signal from the three filters together with an enhanced contribution from the H α intensity map extracted from the line fitting procedure.

The data reduction utilizes the software ORBS (T. Martin et al. 2015), which is specifically developed for SITELLE. L. Rousseau-Nepton et al. (2018) details the full reduction steps. The extraction software ORCS (T. B. Martin et al. 2016), another software developed for SITELLE, is used to fit the sinc-shaped line profiles. L. Rousseau-Nepton et al. (2018) explain how the emission-line regions are detected, giving us flexibility in defining H II regions and their diffuse ionized gas (DIG) background. First, the full data set undergoes sky

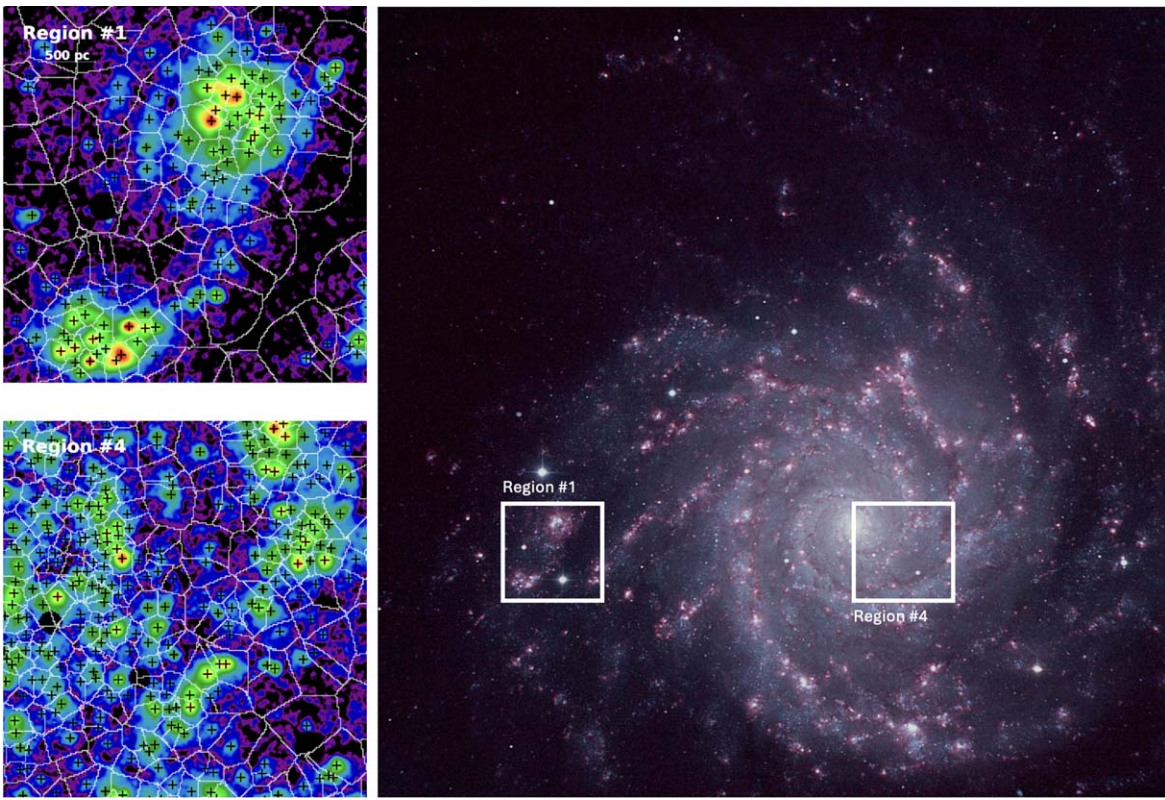


Figure 1. Left panels: regions #1 (top) and #4 (bottom) from L. Rousseau-Nepton et al. (2018, their Figure 7). Each panel shows ionizing sources and their zones of influence drawn over the $\text{H}\alpha + \text{H}\beta + [\text{O III}]$ continuum-subtracted image. The centroid position of each emission peak detected is identified with a cross. The white outlines define the zones of influence surrounding the emission peaks. Each panel measures $\sim 75'' \times 75''$ (3.25 \times 3.25 kpc). Right panel: the deep image of NGC 628 taken with SITELLE (L. Rousseau-Nepton et al. 2018, their Figure 2). For each pixel, the three filters were summed together along with the $\text{H}\alpha$ intensity map which highlights the emission regions in red on the image. The white boxes indicate the positions of Regions #1 and #4. North is up, and east is left. The image measures $11'' \times 11''$ (29 \times 29 kpc).

subtraction, astrometry matching, subtraction of the underlying stellar population, and finally line fitting. The emission peaks are located using a combination of the $\text{H}\alpha$, $\text{H}\beta$, and $[\text{O III}]$ continuum-subtracted image to build up the signal-to-noise ratio (S/N). These peaks are identified when (1) the pixel intensity is greater than the intensity of at least five immediate surrounding pixels, and (2) the total intensity in a 3×3 pixel box centered on the emission peak is above the adopted detection threshold fixed by the 3σ noise level of the flux map. This technique detected a total of 4285 emission peaks. The “zone of influence,” defined by the distance between each pixel and its nearest emission peak, is used to fit a pseudo-Voigt profile where its intensity profile radius determines the size of a region. These region domains are used over the entire data cube. The DIG is then estimated based on the median intensity for all pixels in an annulus 50 pc thick centered on the outer limit of a region and subtracted. The left panel of Figure 1 illustrates this process, showing two regions of NGC 628. The ionizing sources and their zones of influence are drawn over the $\text{H}\alpha + \text{H}\beta + [\text{O III}]$ continuum-subtracted image.

The emission peak catalog of L. Rousseau-Nepton et al. (2018) consists of R.A./decl. coordinates, deprojected radial distances, $\text{H}\alpha$ luminosities, DIG background levels, morphological category, line fluxes, and their associated uncertainties. These line fluxes are corrected for extinction assuming a J. A. Cardelli et al. (1989) extinction curve and Case B recombination (D. E. Osterbrock & G. J. Ferland 2006). We will be using these reddening-corrected line fluxes unless otherwise noted.

Here we apply data quality cuts to select well-detected H II regions. First, an $S/N > 5$ is required for all strong emission lines. We utilize the S/N_{cross} parameter defined by L. Rousseau-Nepton et al. (2018), which takes into account the S/N of two lines simultaneously. Namely, we require that $S/N_{\text{cross}} > 5$ for $[\text{O III}]/\text{H}\beta$, $[\text{O II}]/\text{H}\beta$, $[\text{N II}]/\text{H}\alpha$, and $[\text{S II}]/\text{H}\alpha$. This requirement excludes about 55 % of the regions.

Next, we apply a cut on the BPT (J. A. Baldwin et al. 1981; S. Veilleux & D. E. Osterbrock 1987) diagrams to ensure the emission lines are consistent with photoionization by massive stars. In the $[\text{O III}]/\text{H}\beta$ versus $[\text{N II}]/\text{H}\alpha$ diagram, we require the regions to be consistent with the more stringent G. Kauffmann et al. (2003) empirical line. In the $[\text{O III}]/\text{H}\beta$ versus $[\text{S II}]/\text{H}\alpha$ diagram, the regions must be consistent with the L. J. Kewley et al. (2001) line. This excludes a further $\sim 3\%$.

We require that the uncertainty in the color excess, $E(B - V)$, be < 5 times the value of the color excess. We trim those outliers with extremely high extinction values, requiring $E(B - V) < 0.8$ or $A_V < 2.5$. This excludes another $\sim 6\%$ of the regions. Finally, we require that all emission lines are detected. This final cut excludes only a further five regions. In total, our H II region catalog consists of 1532 H II regions.

In addition to our SIGNALS data for NGC 628, we also include four galaxies from the CHemical Abundances Of Spirals (CHAOS) project, namely NGC 628, M51, M101, and NGC 3184 (D. A. Berg et al. 2015; K. V. Croxall et al. 2015, 2016; D. A. Berg et al. 2020, respectively) totaling 175 H II regions. Using the Multi-Object Double Spectrograph on the Large Binocular Telescope, the CHAOS project is a

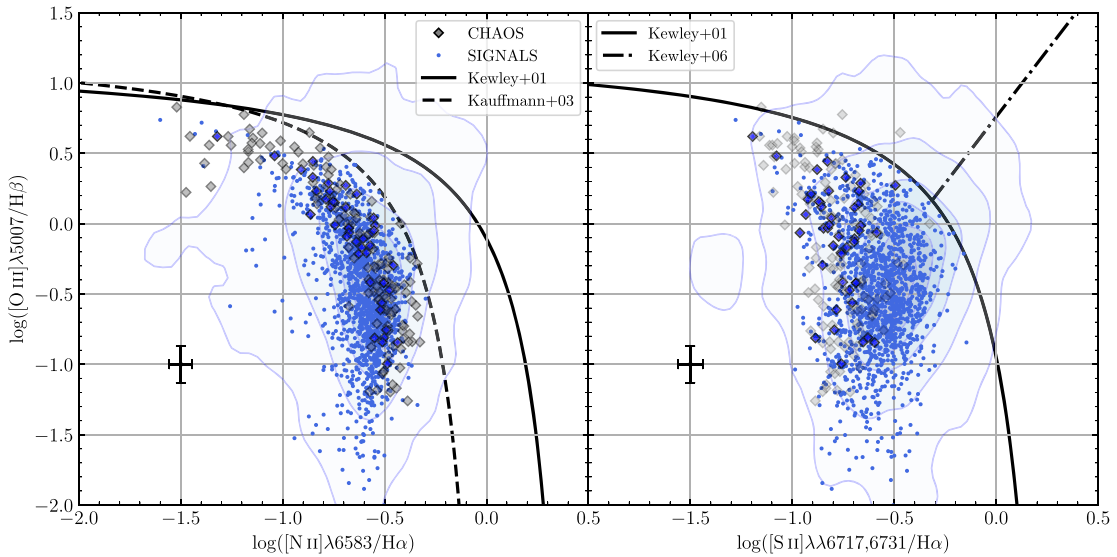


Figure 2. The [N II] (left) and [S II] (right) BPT (J. A. Baldwin et al. 1981; S. Veilleux & D. E. Osterbrock 1987) diagrams for the SIGNALS and CHAOS samples. The SIGNALS data for NGC 628 before any data cuts are shown by the blue contours enclosing 99%, 90%, 70%, 50%, 30%, and 10% from lightest to darkest blue. The remaining H II regions after data cuts are shown by the light-blue points with characteristic error bars shown to the left in each plot. The CHAOS sample consists of the gray diamonds, with those for NGC 628 in dark blue; their uncertainties are smaller than the size of the data point. In the left panel, the dashed line is the pure star formation demarcation from G. Kauffmann et al. (2003). In both panels, the solid line is the extreme starburst demarcation from L. J. Kewley et al. (2001). In the right panel, the dashed-dotted line is the Seyfert/LINER line from L. J. Kewley et al. (2006).

spectroscopic survey of bright H II regions in nearby spiral galaxies. Their continuous and wide spectral coverage (3200–10000 Å), as well as auroral line-based abundance estimates, serves as a useful comparison sample and will be helpful in setting Bayesian priors in Section 4.2.

Figure 2 shows the [N II] and [S II] BPT diagrams for our SIGNALS data set and the CHAOS data set. After the data quality cuts described above, our SIGNALS data for NGC 628 fall in the region of the plots consistent with photoionization by massive stars. As mentioned and performed by L. Rousseau-Nepton et al. (2018), comparing our sample to the CHAOS sample not only demonstrates our ability to reproduce line ratios measured by spectroscopic surveys but also includes objects with a larger range of physical properties (masses, ages, stellar content, interstellar medium (ISM), properties, etc.).

3. A Problem with Ionization Parameter Calibrations?

As mentioned in Section 1, numerous calibrations exist in the literature to estimate the oxygen abundances of H II regions. Detailed analysis of these calibrations has revealed a systematic discrepancy between them, leading to abundance differences of up to 0.5 dex (e.g., L. J. Kewley & S. L. Ellison 2008; J. Moustakas et al. 2010). There appears to be a similar, yet unexplored, issue with the calibrations for the ionization parameter. Several studies have mentioned that existing calibrations differ by an order of magnitude (K. Kreckel et al. 2019; M. Mingozi et al. 2020). However, aside from the pioneering work of X. Ji & R. Yan (2022), who determined the strength of different factors leading to the differences between publicly available photoionization models, the discrepancies between the calibrations have yet to receive equal attention.

Briefly, let us begin with some useful definitions related to the ionization state of the gas in an H II region.¹² Ionic species in H II regions are in ionization equilibrium with the terms

dependent on the properties of the ionizing source and the gas gathered together to define the ionization parameter:

$$\mathcal{U} = \frac{Q_0}{4\pi R_S^2 c n_e}. \quad (1)$$

Here, Q_0 is the production rate of hydrogen-ionizing photons, n_e is the electron density, and c is the speed of light. This is known as the “dimensionless” ionization parameter where the “dimensionful” parameter is usually defined as $q = \mathcal{U}c$ in cm s⁻¹. Here we have made the B. Strömgren (1939) approximation, using the size of a Strömgren sphere, R_S , to define \mathcal{U} . The definition of the Strömgren radius is based on the balance between ionization and recombination rates assuming Case B recombination (D. E. Osterbrock & G. J. Ferland 2006), where

$$R_S = \left(\frac{3Q_0}{4\pi\alpha_B\varepsilon n_H^2} \right)^{1/3} \approx \left(\frac{3Q_0}{4\pi\alpha_B\varepsilon n_e^2} \right)^{1/3}. \quad (2)$$

In the above expression, we assume all of the gas is ionized, so the hydrogen density and electron density are approximately equal, $n_H \approx n_e$. We also introduce the Case B recombination coefficient, α_B , and the volume-filling factor of the gas, ε , defined assuming that the gas is structured in clumps that are surrounded by a lower-density medium, where it is unity for a homogeneous constant-density gas and decreases as the density of clumps increases (R. C. Kennicutt 1984). For simplicity, we can assume $\alpha_B = 2.56 \times 10^{-13} T_4^{-0.83} \text{ cm}^3 \text{ s}^{-1}$, where $T_4 = T_e/10^4 \text{ K}$ (B. T. Draine 2011). This simplifies the ionization parameter to:

$$\mathcal{U} \propto Q_0^{1/3} n_e^{1/3} \varepsilon^{2/3} T_4^{-0.55}. \quad (3)$$

We see that the ionization parameter has a weak dependence on the ionizing photon production and gas density, and is somewhat more dependent on the filling factor and electron temperature.

¹² For more details, the interested reader is referred to the foundational textbooks of D. E. Osterbrock & G. J. Ferland (2006) and B. T. Draine (2011).

However, there are several issues with this common definition of the ionization parameter. While the Strömgren sphere assumption is convenient, it is probably not physically motivated, as it assumes a sphere of constant density that surrounds the ionizing source. However, in real H II regions, feedback from stellar winds carves out a cavity around the ionizing source, making the ionized gas a shell rather than a sphere. Real H II regions also show various complicated substructures and geometries. The Strömgren sphere also assumes that the H II region is radiation-bounded, where no ionizing photons escape, instead of density-bounded.

The main problem is that while it carries useful information about the ionizing source and gas geometry, the ionization parameter is not directly observable. The ionization parameter is instead often estimated using measurements of emission-line ratios that have a sensitivity to the ionization state of the gas, pairs of low- and high-ionization states of the same element, in conjunction with predictions from photoionization models. For instance, the ratios $[O\text{ III}]\lambda\lambda 5007,4959/[O\text{ II}]\lambda 3727$ or $[S\text{ III}]\lambda\lambda 9069,9531/[S\text{ II}]\lambda\lambda 6717,6731$, hereafter O_{32} and S_{32} , respectively, are commonly used since these ratios are good indicators for O^{2+}/O^+ and S^{2+}/S^+ (L. H. Aller 1942; A. I. Díaz et al. 2000; L. J. Kewley & M. A. Dopita 2002; L. J. Kewley et al. 2019).

Since each photoionization model used to calibrate observed line ratios and \mathcal{U} depends on the assumptions inherent to each model, this produces offsets between different calibrations. We investigate these offsets and differences in the O_{32} and S_{32} calibrations using data from SIGNALS and CHAOS, respectively. Namely, we use the calibrations of L. J. Kewley et al. (2019), C. Morisset et al. (2016), O. L. Dors et al. (2011), and A. I. Díaz et al. (2000), hereafter **K19**, **M16**, **D11**, and **D00**, respectively, all of whom have published both O_{32} and S_{32} calibrations. In the case of the calibrations of **K19** where there is a published abundance dependence, we utilized their $[N\text{ II}]/[O\text{ II}]$ abundance calibration, as it has no dependence on the ionization parameter (L. J. Kewley & M. A. Dopita 2002; **K19**). **M16** has published O_{32} calibrations using two different geometries, a thin shell and a filled sphere; we utilize both. Finally, we compare these calibrations to the assumptions of a Strömgren sphere, outlined above. We determine Q_0 empirically from the dust-corrected $H\alpha$ luminosity assuming the relationship of D. E. Osterbrock & G. J. Ferland (2006) and no escape or dust absorption of ionizing photons, i.e.,

$$Q_0 [\text{s}^{-1}] = 7.35 \times 10^{11} L_{H\alpha} [\text{erg s}^{-1}]. \quad (4)$$

To measure the electron density, we used PyNeb (V. Luridiana et al. 2015), considering the ratio of $[S\text{ II}]\lambda 6717/[S\text{ II}]\lambda 6731$ and assuming $T_e = 10^4 \text{ K}$. We fix the volume-filling factor $\varepsilon = 0.01$, a reasonable assumption for H II regions (e.g., R. C. Kennicutt 1984; B. Cedres et al. 2013).

We used a Monte Carlo method to apply these calibrations while including the observational uncertainties associated with the emission-line fluxes by running the calculations for 500 trials assuming Gaussian uncertainties. In this way, we take the median of these 500 trials as the estimate of \mathcal{U} and the standard deviation as the uncertainty on \mathcal{U} . Figure 3 shows the $\log O_{32}$ – $\log \mathcal{U}$ calibrations from the literature applied to the SIGNALS data set on the top, and the $\log S_{32}$ – $\log \mathcal{U}$ calibrations applied to the CHAOS data set on the bottom. Reported in each plot are the median and quartiles for each calibration.

Looking first at the $\log O_{32}$ – $\log \mathcal{U}$ calibrations in Figure 3, we see that the data at low $\log O_{32}$ flares away from the calibration lines in each case. These data have very large uncertainties in $\log O_{32}$, upward of 2 dex caused by large uncertainties in $[O\text{ III}]$, which results in large uncertainties on the $\log \mathcal{U}$ values, ~ 0.6 dex, due to the random Monte Carlo sampling. However, most of our data points lie along the calibration line. The median values of $\log \mathcal{U}$ for the calibrations are approximately the same at $\log \mathcal{U} \simeq -3.5$ with **K19** and **D11** predicting slightly higher values. Interestingly, the **M16** filled sphere calibration predicts much lower values of $\log \mathcal{U} \simeq -4.3$, which disagrees strongly with the Strömgren sphere estimation. Much more concerning is that none of the calibrations exactly agree with one another. The disagreement is likely caused by the O_{32} ratio's strong dependence on the metallicity as well as ISM pressure in metal-rich galaxies (L. J. Kewley & M. A. Dopita 2002; **K19**) since only some models control for these dependencies.

The $\log S_{32}$ – $\log \mathcal{U}$ calibrations do not fare much better. This is especially concerning given that all of the CHAOS H II regions are the bright, massive, and young H II regions easily accessible by most surveys. The S_{32} ratio is frequently claimed to be a better estimation of the ionization parameter than O_{32} , as it lacks a dependency on metallicity. However, comparing the median values between $\log O_{32}$ and $\log S_{32}$ calibrations shows a higher scatter between $\log S_{32}$ – $\log \mathcal{U}$ calibrations than between $\log O_{32}$ – $\log \mathcal{U}$ calibrations. The historical difficulty that photoionization codes have had reproducing the strengths of the far-red [S III] lines might cause the higher scatter. This difficulty was a result of a lack of an accurate estimate of the dielectronic recombination coefficient for the transition $S^{2+} \rightarrow S^+$ (Y. I. Izotov et al. 2009; F. Belfiore et al. 2022). Recent updates to the photoionization code CLOUDY (M. Chatzikos et al. 2023) have fixed this, resulting in an increase in the predicted flux of the [S II] lines and a decrease in S_{32} by 20%–50% at a fixed O_{32} (N. R. Badnell et al. 2015). These changes could explain why the $\log S_{32}$ – $\log \mathcal{U}$ calibration of **K19** predicts a lower $\log \mathcal{U}$ more in line with the $\log O_{32}$ – $\log \mathcal{U}$ calibrations than the others.

Table 1 shows that each calibration is derived from photoionization models with different built-in assumptions and modeling codes. X. Ji & R. Yan (2022) performed an extensive analysis on a different set of publicly available photoionization models. They found three major factors contributing to the differences among those models: updated atomic data (mentioned above), the stellar spectral energy distribution (SED), and the gas-phase chemical abundance set. Broadly speaking, we find the same important differences in these models. We refer the interested reader to the excellent discussion of X. Ji & R. Yan (2022) but briefly mention a few key points particular to these models.

The stellar SED determines the relative number of ionizing photons and helps set the emission-line ratios. Most of the models use well-established and recent STARBURST99 or PopStar SEDs, which, at least for the timescales necessary for H II regions, produce similar numbers of ionizing photons between them (M. Mollá et al. 2009). The lone exception is the calibration of **D00**, which uses the models of A. I. Díaz et al. (1991). These models utilized single-star models with atmospheres taken from D. Mihalas (1972). Aside from this not being physically correct for H II regions consisting of ionizing star clusters of different ages, earlier work showed that these stellar

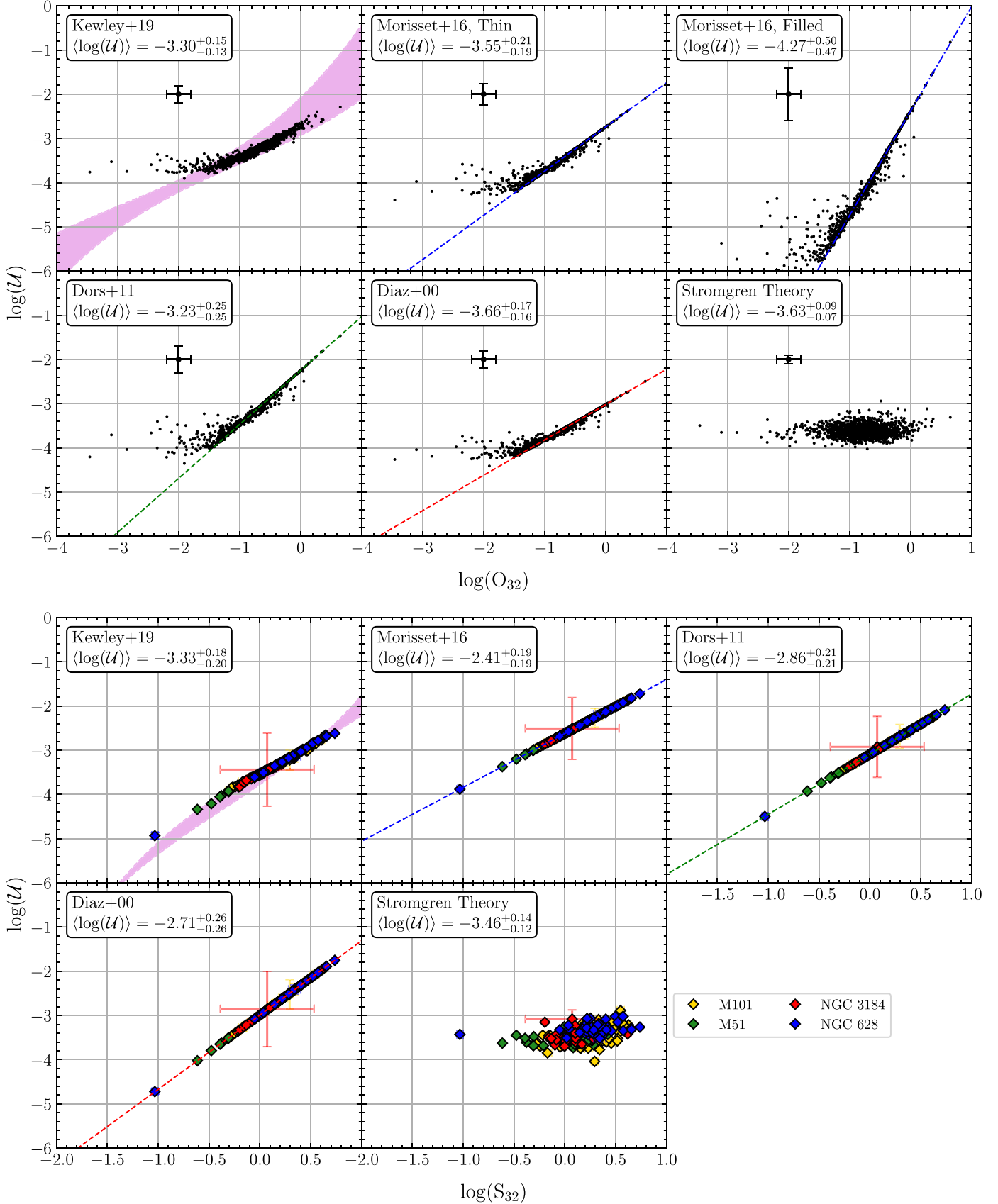


Figure 3. $\log \mathcal{U}$ calibrations from the literature. The top group of six panels shows the $\log O_{32}$ – $\log \mathcal{U}$ calibrations applied to the SIGNALS data. Characteristic error bars are shown in the upper left. The bottom group of five panels shows the $\log S_{32}$ – $\log \mathcal{U}$ calibrations applied to the CHAOS data. Colors indicating different CHAOS galaxies are indicated in the legend. Individual error bars are shown, often smaller than the size of the data point. Each panel shows a different calibration given in the legend as well as the median and quartiles for each calibration.

Table 1
Input Parameters for Literature Photoionization Models

Parameter	Values
K19 Model (L. J. Kewley et al. 2019)	
Photoionization Code	MAPPINGS v5.1 (R. Sutherland et al. 2018)
$\log \mathcal{U}$	-4, -3.75, -3.5, -3.25, -3, -2.75, -2.5, -2.25, -2
$\log(Z/Z_{\odot})$	-1.06, -0.46, -0.16, 0.24, 0.54
$\log(n_{\text{H}}/\text{cm}^{-3})$	1
Geometry	Plane-parallel
Stellar SED	STARBURST99 v7 (C. Leitherer et al. 2014)
Solar Abundance Set	D. C. Nicholls et al. (2017)
Nitrogen Prescription	D. C. Nicholls et al. (2017)
Dust Depletion Factor	E. B. Jenkins (2009)
M16 Model (C. Morisset et al. 2016)	
Photoionization Code	CLOUDY v13.03 (G. J. Ferland et al. 2013)
$\log \mathcal{U}$	-4, -3.75, -3.5, -3.25, -3, -2.75, -2.5, -2.25, -2, -1.75, -1.5
$\log(Z/Z_{\odot})$	-0.53 to 0
$\log(n_{\text{H}}/\text{cm}^{-3})$	1
Geometry	Plane-parallel and Spherical
Stellar SED	POPSTAR (M. Mollá et al. 2009)
Solar Abundance Set	M. Asplund et al. (2009)
Nitrogen Prescription	$\log(\text{N}/\text{O})$: -1.5, -0.75, 0, 0.75, 1.5
Dust Depletion Factor	Default depletion set in CLOUDY (L. L. Cowie & A. Songaila 1986; E. B. Jenkins 1987)
D11 Model (O. L. Dors et al. 2011)	
Photoionization Code	CLOUDY v8.00 (last described in G. J. Ferland et al. 1998)
$\log \mathcal{U}$	-3.5, -3, -2.5, -2, -1.5
$\log(Z/Z_{\odot})$	-1.3, -0.7, -0.4, -0.2, 0, 0.3
$\log(n_{\text{H}}/\text{cm}^{-3})$	2.3
Geometry	Plane-parallel
Stellar SED	STARBURST99 v6 (C. Leitherer et al. 2010)
Solar Abundance Set	C. Allende Prieto et al. (2001)
Nitrogen Prescription	M. B. Vila-Costas & M. G. Edmunds (1993)
Dust Depletion Factor	D. R. Garnett et al. (1995)
D00 Calibration (A. I. Díaz et al. 2000) Using the Models of A. I. Díaz et al. (1991)	
Photoionization Code	CLOUDY v74 ^a (G. J. Ferland 1989)
$\log \mathcal{U}$	-4, -3.5, -3, -2.5
$\log(Z/Z_{\odot})$	0 and 0.3
$\log(n_{\text{H}}/\text{cm}^{-3})$	1
Geometry	Spherical
Stellar SED	Single-star models of D. Mihalas (1972)
Solar Abundance Set	G. Stasińska (1990)
Nitrogen Prescription	Unspecified
Dust Depletion Factor	Unspecified

Note.

^a A. I. Díaz et al. (1991) did not specify which version of CLOUDY they used. However, it should be no later than v74 according to the code release information at <https://gitlab.nublado.org/cloudy/cloudy/-/wikis/CloudyOld>.

atmospheres are unsuitable for modeling H II regions due to their lack of treatment for heavy element bound-free opacity (J. Borsenberger & G. Stasińska 1982; I. N. Evans 1991). Despite these strong cautions, the D00 calibration does show a remarkable agreement with the others considered here. Perhaps another model parameter offsets the issues caused by these softer SEDs.

The chemical abundances are fundamental for setting the line ratios emitted by the H II regions. While four separate solar abundance sets are used, these are further modified by the

chosen nitrogen prescription, i.e., the relation between the N/O ratio and metallicity, and the dust depletion factors. The chemical abundance sets and nitrogen prescriptions of each of the four models in Table 1 are approximately the same: the nitrogen prescriptions of D. C. Nicholls et al. (2017) and M. B. Vila-Costas & M. G. Edmunds (1993) used by K19 and D11, respectively, differ only in the low-metallicity regime by about 0.2 dex. Meanwhile M16 uses the N/O ratio as an input parameter, and it is unclear what, if any, nitrogen prescription the models of D00 used.

The chosen dust depletion factors also have an important effect on the emitted spectrum of an H II region. Dust depletion has two effects: reducing the intensities of the lines emitted by depleted elements, and strengthening the lines emitted by nondepleted elements as the removed coolants raise the equilibrium temperature. All of the dust depletion models deplete oxygen by varying degrees, the E. B. Jenkins (2009) depletion factors used by K19 model depletes nitrogen, and none deplete sulfur.¹³ While this would suggest that the dust depletion should not affect the $\log S_{32}$ - $\log \mathcal{U}$ calibrations, removing other elemental coolants will strengthen the remaining emission lines, making the model spectrum appear more highly ionized. Perhaps this explains some of the differences observed in the $\log S_{32}$ - $\log \mathcal{U}$ calibrations, while the differences observed in the $\log O_{32}$ - $\log \mathcal{U}$ calibrations are more intertwined with other model factors.

In summary, the atomic data, the stellar SED, and the final gas-phase chemical abundance set are likely responsible for the differences between these models and their resulting ionization parameter calibrations. Unfortunately, without publicly available model grids or detailed descriptions of the model inputs, further analysis makes it difficult to say which, if any, of these three input parameters is most responsible. As X. Ji & R. Yan (2022) mention, there is also the possibility of degeneracies between these three inputs: a harder stellar SED might cancel out the underestimation of elemental abundances or overestimation of depletion factors. Therefore, using these published calibrations is ill-advised without understanding the assumptions inherent in their models.

4. Photoionization Models and Parameter Estimation

Additionally, the most popular line ratio used to estimate $\log \mathcal{U}$ and the one directly available to us, O_{32} , has a secondary dependence on metallicity (L. J. Kewley & M. A. Dopita 2002). Since we wish to explore the correlation between oxygen abundance and ionization parameter, instead of adopting any particular calibrator for each, we choose to estimate \mathcal{U} and $12 + \log(\text{O}/\text{H})$ for each of our H II regions in a self-consistent way, i.e., through our photoionization modeling. This way, we can avoid mixing the uncertainties between two calibration assumptions, one for \mathcal{U} and another for $12 + \log(\text{O}/\text{H})$. The details of our photoionization models and our estimation of individual H II regions' parameters are described below.

4.1. CLOUDY Models

We used the photoionization code CLOUDY v23.01 (M. Chatzikos et al. 2023). The input SED for the models were computed using the code STARBURST99 (C. Leitherer et al. 2014). We assume a P. Kroupa (2001) IMF, and a fixed

¹³ It remains an open question whether or not sulfur depletes in the ISM. See E. B. Jenkins (2009) for a discussion.

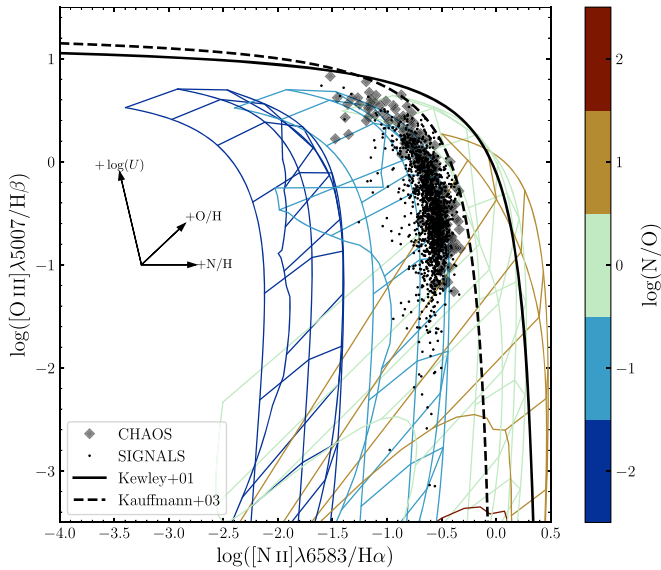


Figure 4. The [N II] BPT diagram for the SIGNALS (black dots) and CHAOS (gray diamonds) samples with a subset of our photoionization models overlaid. The models are colored by their N/O ratios. Arrows are given to indicate in which direction $\log U$, O/H, and N/H increase. Demarcation lines from G. Kauffmann et al. (2003) and L. J. Kewley et al. (2001) are shown as dotted and solid black lines, respectively.

total mass of $10^7 M_{\odot}$ over 100 Myr, selecting the SED at 2.5 Myr as the SED for our H II regions. From previous studies, NGC 628 has H II regions with a gas-phase abundance of approximately solar (e.g., M. L. McCall et al. 1985; A. M. N. Ferguson et al. 1998; S. F. Sánchez et al. 2011; H. Zou et al. 2011; D. A. Berg et al. 2015). Making the reasonable assumption of a tight link between the gas-phase abundance and stellar-phase abundance of the ionizing stars, i.e., recently formed OB stars, we only utilized SEDs with solar stellar abundances, $Z_{\odot} = 0.02$. When computing these SEDs, we used the A. W. A. Pauldrach et al. (2001) and D. J. Hillier & D. L. Miller (1998) stellar atmospheres and the high mass-loss Geneva evolutionary tracks (G. Meynet et al. 1994).

We set the hydrogen density of the ionized gas cloud to 100 cm^{-3} , which is the median electron density calculated from the ratio of the [S II] lines, and assume an electron temperature of 10^4 K . The gas pressure is considered to be constant throughout the cloud. We include dust grains with typical ISM abundance, which we scale with the metallicity of the cloud. Metal depletion onto the dust grains is computed using the values given by L. L. Cowie & A. Songaila (1986) and E. B. Jenkins (1987). The solar abundance we use is taken from N. Grevesse et al. (2010) with $12 + \log(\text{O/H})_{\odot} = 8.69$. We scale all other elements with oxygen except nitrogen, carbon, and sulfur. We let the nitrogen abundance be a free parameter in our models while we adopt the C/O prescription of M. A. Dopita et al. (2013). We refit these data using a simple quadratic function:

$$\text{C/H} = 0.249 \times (\text{O/H})^2 + 3.515 \times \text{O/H} + 5.322. \quad (5)$$

For sulfur, we adopt the S/O prescription of D. A. Berg et al. (2020), who found a constant $\log(\text{S/O}) = -1.34 \pm 0.15$. This value differs from the solar value by about 0.23 dex (N. Grevesse et al. 2010).

To set up a grid, we vary the cloud’s ionization parameter, oxygen abundance, and nitrogen abundance. The ranges we

adopt for each are $-5 \leq \log U \leq -1.5$ in 0.1 dex steps, $-4.5 \leq \log(\text{O/H}) \leq -2.5$ in 0.1 dex steps, and $-6.5 \leq \log(\text{N/H}) \leq -2.5$ in 0.25 dex steps. This results in 12,852 total models. Figure 4 shows a subset of our models on the [N II] BPT diagram and how they overlap with both the SIGNALS and CHAOS data. Evident from this figure is that our models cover the emission-line space occupied by our data well, except for a few very-high-ionization regions. Additionally, we can easily read off the plot that most of our data (78%) has $-1 \lesssim \log(\text{N/O}) \lesssim 0$, which is consistent with the CHAOS N/O ratios measured using direct abundances (D. A. Berg et al. 2020).

4.2. Extracting Properties with NebulaBayes

Given the relatively large parameter space outlined above, we need a method that efficiently estimates the parameters for each H II region in our sample. We use the Bayesian analysis code NebulaBayes (A. D. Thomas et al. 2018), chosen as it is a generalization of two previous Bayesian codes IZI (G. A. Blanc et al. 2015) and BOND (N. Vale Asari et al. 2016). While it comes with a pre-made model grid for H II regions (A. D. Thomas et al. 2018), NebulaBayes is entirely customizable, allowing for custom model grids, error weighting, choice of priors, and choice of lines that influence the likelihood distribution, among others. Given this information and observed emission-line fluxes, NebulaBayes returns an inferred value and uncertainty for each property varied in the model grid. This code has been used extensively in estimating active galactic nucleus properties (e.g., M. Radovich et al. 2019; A. D. Thomas et al. 2019; H. R. M. Zovaro et al. 2020; B. Pérez-Díaz et al. 2021; M. S. Polimera et al. 2022; G. Peluso et al. 2023; S.-L. Li et al. 2024), but little work has used it to estimate the properties of H II regions (e.g., C. Espinosa-Ponce et al. 2022; S.-L. Li et al. 2024). As such, an extensive investigation into the proper choice of NebulaBayes parameters is necessary.

Here, we investigate three NebulaBayes parameters: error weighting, choice of lines that influence the likelihood distribution, and choice of priors. In order to compare our model properties with observed properties, we use the CHAOS data set, which has emission-line fluxes, including the [S III] lines, and measured oxygen and nitrogen abundances. However, it is important to remember that the measured abundances come from electron temperature measurements, which are offset by as much as 0.5 dex from photoionization grid abundances (e.g., J. Moustakas et al. 2010).

First, we pick how the errors on the observed line fluxes are weighted. Normally, one would simply use the observed line flux uncertainties as the weights, but due to the changing resolution across the three SITELLE filters ($R \simeq 600$ in SN1 and SN2 and $R \simeq 1800$ in SN3; L. Rousseau-Nepton et al. 2018), the observed uncertainties change with wavelength as well. The median [O II] and [O III] uncertainties in the SIGNALS data set are $\sim 30\%$, while those of [S II] and [N II] are $\sim 15\%$ and $\sim 10\%$, respectively, despite the weaker line flux. Compare this to CHAOS, for which the uncertainties are approximately uniform across wavelength at $\sim 1\%$ —as such, using just the observed uncertainties as the weights would shift the NebulaBayes solution toward models that match the [N II] and [S II] lines at the expense of the oxygen lines. Therefore, we choose to adopt, for all of the SITELLE lines, a 10% error as the input observational errors for NebulaBayes to match our most well-determined emission lines.

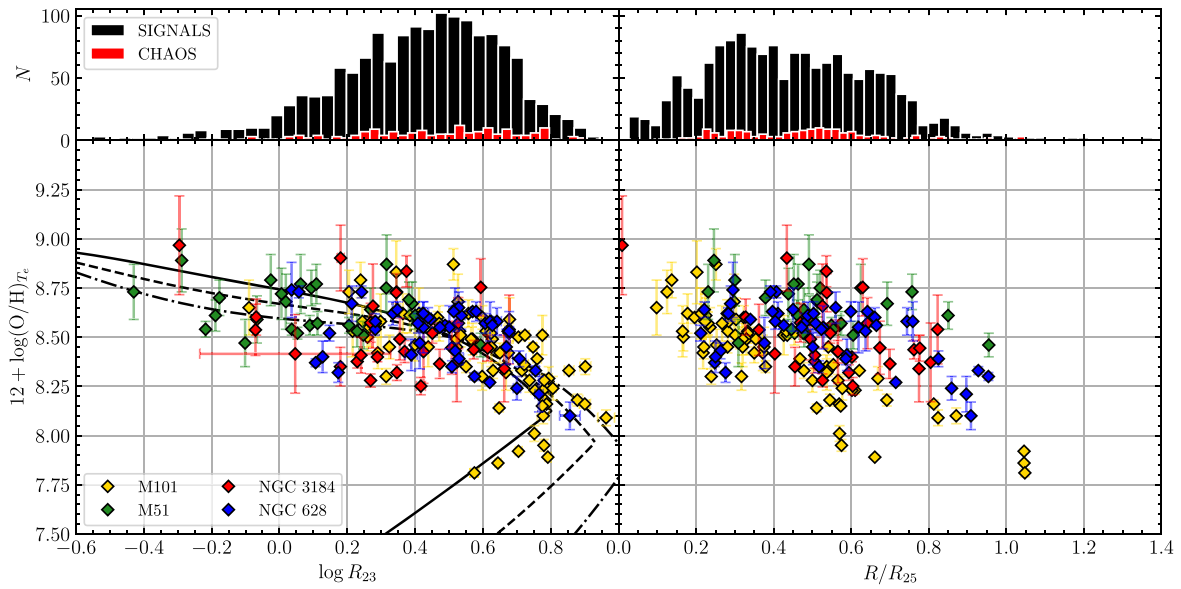


Figure 5. Left panel: the R_{23} –O/H relation for the CHAOS data. Included is the R_{23} prescription of H. A. Kobulnicky & L. J. Kewley (2004) for comparison, shifted down by 0.5 dex to lie on the CHAOS data. The different lines represent different $\log U$: –4 (solid), –3 (dashed), and –2 (dashed-dotted). Right panel: the oxygen abundance gradients for the CHAOS data. In both panels, the colors are the same as in Figure 3. At the top of both panels are histograms comparing the R_{23} and R_{25} distributions of the CHAOS (red) and SIGNALS (black) data.

Second, we choose which observed emission lines influence the likelihood distribution. We chose to output our modeled emission lines as fractions of $\text{H}\beta$, and because we have already corrected our data for extinction, the hydrogen lines $\text{H}\alpha$ and $\text{H}\beta$ do not provide any additional constraining power. We do not include these lines in the likelihoods. We must include the [N II], [O II], and [O III] emission lines since ratios between these lines, i.e., $[\text{N II}]/[\text{O II}]$, $R_{23} = ([\text{O III}]+[\text{O II}])/\text{H}\beta$, and $O_{32} = [\text{O III}]/[\text{O II}]$, are proxies for N/H, O/H, and U , respectively (e.g., B. E. J. Pagel et al. 1979; L. J. Kewley & M. A. Dopita 2002; H. A. Kobulnicky & L. J. Kewley 2004).

Ultimately, we decided against including the sulfur lines in the likelihoods for a few reasons. First, [S II] comes from the outskirts of an H II region, which does not coincide with the production sites of other strong lines (e.g., see Figure 1 and discussion of F. Mannucci et al. 2021). Second, any density structure in the H II region will change the strength of [S II] with respect to the other lines, and our CLOUDY models assume a constant electron density throughout the entirety of the modeled H II region. Similarly, while we usually assume that the S/O ratio is constant (D. R. Garnett et al. 1997; Y. I. Izotov et al. 2006; D. A. Berg et al. 2020), recent work has questioned that assumption, finding S/O decreases with increasing O/H (J. M. Vilchez et al. 1988; O. L. Dors et al. 2016; A. I. Díaz & S. Zamora 2022), perhaps due to different production sites of sulfur and oxygen (S. Goswami et al. 2024). Additionally, there are known problems with matching the [S II] and [S III] fluxes with photoionization models. The [S II] lines are generally weaker by ~ 0.1 dex than observed (E. M. Levesque et al. 2010; M. A. Dopita et al. 2013; M. Mingozi et al. 2020). The discrepancy between observed and modeled [S III] fluxes has been well reported in the literature (e.g., H. L. Dinerstein & G. A. Shields 1986; D. R. Garnett 1989; B. Ali et al. 1991), and is likely caused by limitations in modeling stellar atmospheres and/or in the atomic data for sulfur (D. R. Garnett 1989; N. R. Badnell et al. 2015).

Finally, we select the priors. NebulaBayes is very flexible in the shape of the priors, and we choose to use the “line-ratio

prior” feature. In this case, NebulaBayes calculates a prior over the entire model grid based on the ratio of a pair of lines. We implement a custom “line-sum prior” for the R_{23} . Numerous studies have used some combination of these or other line ratios as priors (e.g., N. Vale Asari et al. 2016; A. D. Thomas et al. 2018; M. Mingozi et al. 2020; S.-L. Li et al. 2024).

Since we are utilizing several strong line ratios, in particular R_{23} , which is well known to be double-valued with oxygen abundance, this set of priors will return double-valued abundance solutions. In order to break this degeneracy, we must rely on assumptions about how the oxygen abundance behaves in the galaxy. Using the CHAOS data as a comparison in Figure 5, the metal-rich branch of the R_{23} –O/H relation is preferred up to large radii, $R < 0.8R_{25}$. Data outside this radial range would prefer the metal-poor branch, but this radial range accounts for only $\sim 5\%$ of our SIGNALS data for NGC 628, so we can safely assume that most of the H II regions in our sample will lie on the upper, metal-rich branch. Therefore, we convolve an additional Gaussian prior on the oxygen abundance, $\mathcal{N}(9, 0.5)$, to select the metal-rich solution from NebulaBayes. We stress that this additional prior does not force the solutions to have oxygen abundances of 9 but simply skews the posteriors to favor the metal-rich solution. A similar technique, albeit done on a region-to-region basis, was used by A. L. Strom et al. (2018) on their sample of high-redshift galaxies.

Figure 6 shows how the resulting derived line ratios and physical properties compare to those obtained by CHAOS. The $[\text{N II}]/[\text{O II}]$ and O_{32} ratios agree very well, as does the R_{23} up to about $\log(R_{23}) \sim 0.7$. We are likely seeing the effect of forcing these regions to lie on the upper, metal-rich branch of the R_{23} –O/H relation since, at these R_{23} values, they would no longer be metal-rich. Most of these regions are in M101, but those few in NGC 628 lie at radii greater than $R > 0.8R_{25}$. Again, this only accounts for 5% of our SIGNALS data, so it is likely that most of the galaxy lies on the metal-rich branch. Meanwhile, the line ratio S_{32} broadly agrees between our models and CHAOS, although with a considerably large

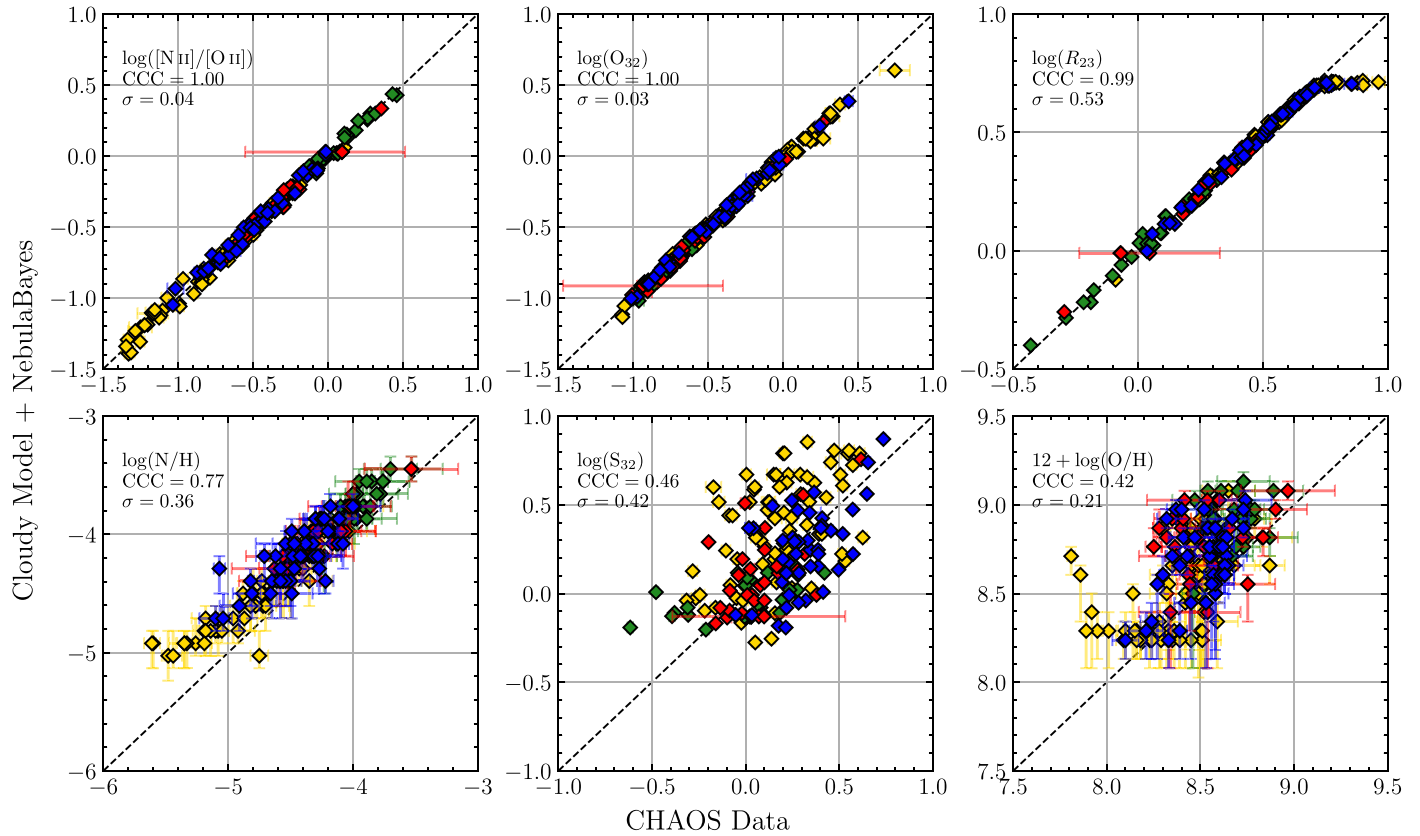


Figure 6. Each panel compares the values of one property between that measured by CHAOS on the x -axis and our model grid through NebulaBayes on the y -axis. The properties compared are labeled inside each panel. Colors are the same as in Figure 3: M101 is gold, M51 is green, NGC 3184 is red, and NGC 628 is blue. In all panels, error bars are shown for the CHAOS data, while NebulaBayes only returns uncertainties for the nitrogen and oxygen abundances. The CCC (concordance correlation coefficient; L. I.-K. Lin 1989), which measures the deviation of a relationship from the 1:1 line (where +1 is a perfect agreement and -1 is a perfect disagreement), is reported as well as the scatter, σ .

scatter. This is expected since we have removed the sulfur lines' constraining power from our analysis. The nitrogen abundance agrees well within the uncertainties except at very low nitrogen abundance. Finally, we find that the oxygen abundance broadly agrees, though our models show a distinct offset toward higher abundances. This is expected, since this comparison involves electron temperature abundances and photoionization model abundances, which are known to be discrepant (L. J. Kewley & S. L. Ellison 2008; J. Moustakas et al. 2010).

Given the above analysis, and especially the comparisons in Figure 6, we are confident that we can use NebulaBayes to estimate reasonable physical properties of H II regions. In the next Section, we apply NebulaBayes to the SIGNALS data set for NGC 628 and investigate the bulk properties and correlations of its H II regions.

5. Recovering Gradients in NGC 628

Using the priors, lines, and observed line errors described in the previous Section, we apply the NebulaBayes algorithm to our SIGNALS data set. We also convolve the posterior distributions of the nitrogen and oxygen abundances to estimate the N/O ratio for our data set.

In the case of the N/O ratio, 63 (4%) H II regions have unbound posteriors and are treated as upper limits. These regions are unbound in only N/O and are bound in the other three parameters. However, they are at the upper ends of the

nitrogen and oxygen abundance distributions, so it is likely that these regions have nonzero N/O ratios but are simply badly fit by a combination of the model grid and NebulaBayes. Calculating the N/O ratios for this set of regions by subtracting the nitrogen and oxygen abundances gives N/O ratios of approximately the solar value, bringing them in line with the rest of the distribution. Therefore, we choose to include these regions with unbound N/O posteriors in our analysis.

The interquartile ranges in the model parameters for this subsample, including those with upper limits on N/O, are

$$\begin{aligned} 12 + \log(O/H) &= [8.61, 8.92], \\ \log \mathcal{U} &= [-3.07, -2.79], \\ \log(N/H) &= [-4.39, -4.08], \text{ and} \\ \log(N/O) &= [-0.84, -0.37]. \end{aligned}$$

These characteristic ranges are consistent with ranges from inferences of these parameters by other means (F. F. Rosales-Ortega et al. 2011; S. F. Sánchez et al. 2015; C. Espinosa-Ponce et al. 2022), as is discussed next.

Figure 7 shows the O₃₂–log \mathcal{U} and S₃₂–log \mathcal{U} calibrations in the left and right panels, respectively. In the left panel, we use a quadratic function to fit individual H II regions from the SIGNALS data set. In the right panel, we fit H II regions from the CHAOS data set using a linear function. Both functional fits and their scatters and C. Spearman (1904) correlation coefficients are given in Table 2. Also shown in both panels

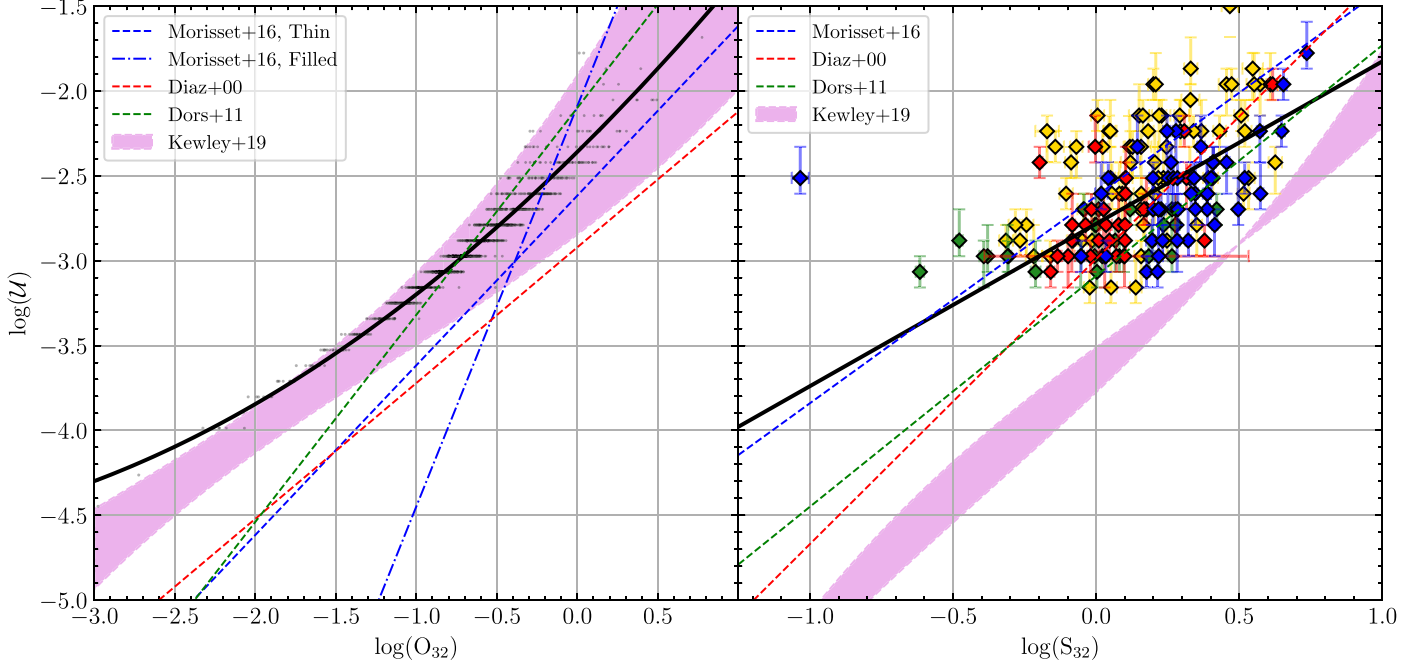


Figure 7. Left panel: the O_{32} - $\log \mathcal{U}$ calibration for the H II regions in NGC 628 for SIGNALS. Individual H II regions are shown as small black points that are in 0.1 dex bins in $\log \mathcal{U}$. The solid black line is the fit to the SIGNALS data, while the colored lines and bands are calibrations from the literature. Right panel: the S_{32} - $\log \mathcal{U}$ calibration of the H II regions in CHAOS. The colors are the same as in Figure 3. The solid black line is the fit to the CHAOS data, while the colored lines and bands are calibrations from the literature. See the text for more details.

Table 2
Fit to Gradients and Calibrations

y	x	Equation	σ_{raw}	σ_{bin}	ρ_{raw}	p_{raw}	ρ_{bin}	p_{bin}
$\log \mathcal{U}$	$\log O_{32}$	$y = +(0.10 \pm 0.01)x^2 + (0.93 \pm 0.02)x - (2.36 \pm 0.01)$	0.07	...	+0.98	4.9×10^{-22}
$\log \mathcal{U}$	$\log S_{32}$	$y = +(0.96 \pm 0.09)x - (2.78 \pm 0.02)$	0.29	...	+0.53	4.8×10^{-14}
$12 + \log(O/H)$	R/R_{25}	$y = -(0.65 \pm 0.06)x + (9.04 \pm 0.05)$	0.15	0.09	-0.75	1.3×10^{-35}	-0.93	5.8×10^{-7}
$\log \mathcal{U}$	R/R_{25}	$y = +(0.53 \pm 0.14)x - (3.20 \pm 0.11)$	0.30	0.16	+0.31	2.4×10^{-35}	+0.63	1.2×10^{-2}
$\log(N/O)$	R/R_{25}	$y = -(1.07 \pm 0.09)x - (0.18 \pm 0.07)$	0.23	0.13	-0.78	1.6×10^{-35}	-0.95	9.5×10^{-8}
$\log \mathcal{U}^a$	$12 + \log(O/H)$	$y = -(0.50 \pm 0.09)x + (1.50 \pm 0.76)$	0.30	0.12	-0.21	6.8×10^{-17}	-0.83	3.7×10^{-6}
$\log \mathcal{U}^b$	$12 + \log(O/H)$	$y = -(0.67 \pm 0.08)x + (3.05 \pm 0.68)$	0.31	0.09	-0.46	2.7×10^{-40}	-0.94	4.5×10^{-9}
$12 + \log(O/H)^a$	$E(B-V)$	$y = +(0.11 \pm 0.05)x + (8.75 \pm 0.02)$	0.22	0.08	+0.11	2.2×10^{-5}	+0.53	5.4×10^{-2}
$12 + \log(O/H)^b$	$E(B-V)$	$y = +(0.19 \pm 0.07)x + (8.76 \pm 0.03)$	0.22	0.06	+0.22	3.3×10^{-9}	+0.55	4.3×10^{-2}
$\log \mathcal{U}^a$	$E(B-V)$	$y = -(0.61 \pm 0.08)x - (2.76 \pm 0.03)$	0.30	0.06	-0.30	2.4×10^{-32}	-0.95	6.1×10^{-8}
$\log \mathcal{U}^b$	$E(B-V)$	$y = -(0.65 \pm 0.11)x - (2.70 \pm 0.05)$	0.30	0.08	-0.38	7.7×10^{-27}	-0.86	3.8×10^{-5}
$12 + \log(O/H)^a$	$\log \Sigma_{\text{H}\alpha}$	$y = +(0.02 \pm 0.02)x + (8.15 \pm 0.65)$	0.22	0.09	+0.13	8.4×10^{-7}	+0.28	2.8×10^{-1}
$12 + \log(O/H)^b$	$\log \Sigma_{\text{H}\alpha}$	$y = -(0.01 \pm 0.02)x + (9.30 \pm 0.66)$	0.22	0.07	+0.05	1.8×10^{-1}	-0.15	6.3×10^{-1}
$\log \mathcal{U}^a$	$\log \Sigma_{\text{H}\alpha}$	$y = +(0.01 \pm 0.03)x - (3.42 \pm 1.01)$	0.31	0.11	+0.09	2.8×10^{-4}	+0.13	6.2×10^{-1}
$\log \mathcal{U}^b$	$\log \Sigma_{\text{H}\alpha}$	$y = +(0.04 \pm 0.03)x - (4.59 \pm 1.00)$	0.30	0.11	+0.03	3.6×10^{-1}	+0.41	1.7×10^{-1}

Notes. Fits to various relations in this paper. The y and x variables are given in the first two columns. The resulting best fit is given in Column (3) with uncertainties on all coefficients. Columns (4) and (5) list the residual scatter in the raw unbinned data, σ_{raw} , and in the binned data, σ_{bin} . Columns (6) and (7) list the Spearman correlation coefficient, ρ , and corresponding p -value for the raw unbinned data, while Columns (8) and (9) list the same for the binned data.

^a Fitted to all H II regions.

^b Fitted to only H II regions with $H\alpha$ S/N ≥ 15 .

are the calibrations from Section 3. Most of the linear calibrations only match our data at high O_{32} with approximately the same slope. In contrast, the filled sphere prescription of M16 does not match our data at all. The calibration of K19 agrees best with nearly all of our H II regions lying within their band of models with a small deviation at low $\log \mathcal{U}$.

The right panel of Figure 7 presents the S_{32} - $\log \mathcal{U}$ calibration for the CHAOS data set since this data set has the [S III] lines. In stark contrast with the left panel, we see that only the calibration presented by K19 disagrees with the data. It

is unknown what causes this disagreement, although it could be related to some of the model assumptions discussed in Section 3, particularly the atomic data. What is more apparent is the large amount of scatter seen in the CHAOS data, whereas other studies have generally shown a tight correlation with little scatter between S_{32} and $\log \mathcal{U}$ (A. I. Díaz et al. 1991; L. J. Kewley & M. A. Dopita 2002; D11; M16). However, the large scatter observed here is likely due to our NebulaBayes algorithm not using the sulfur lines to constrain $\log \mathcal{U}$. Adding the sulfur lines into NebulaBayes would require including a

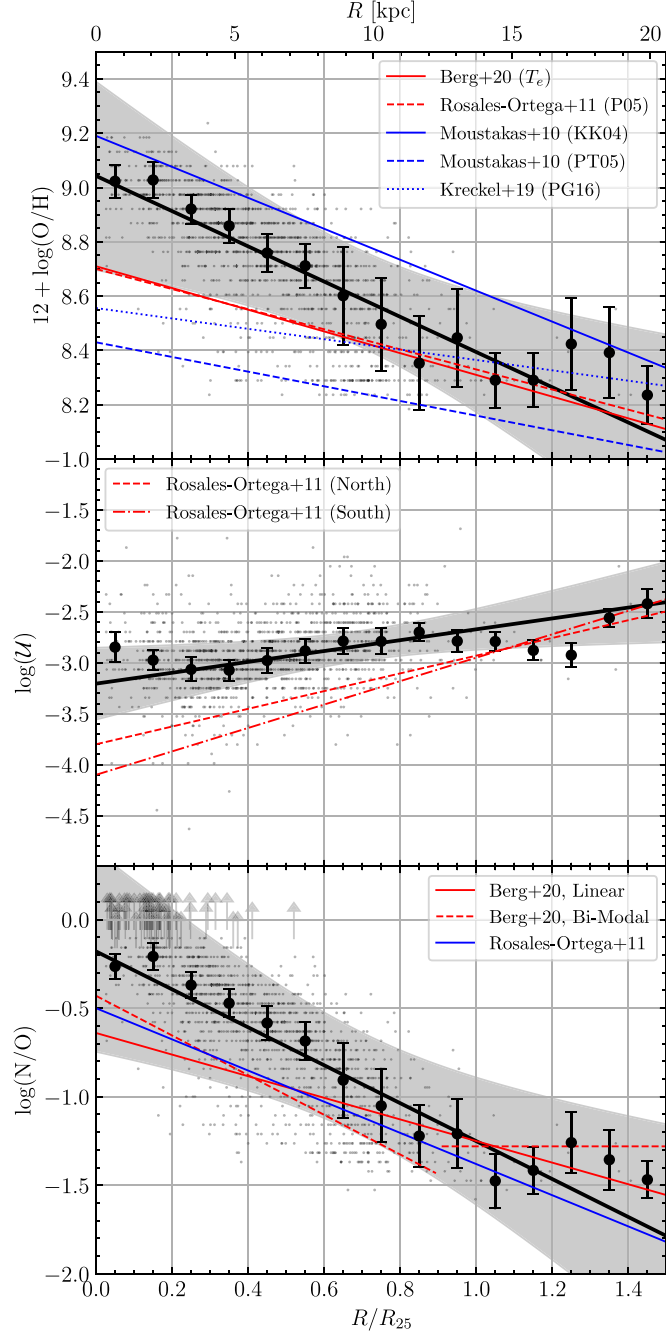


Figure 8. Physical parameter radial gradients in NGC 628. In all panels, individual H II regions are small black points that are binned in radius of width $0.1R_{25}$, as the large black points with error bars. The solid black line is a fit to the binned data with the shaded region being the 1σ uncertainty to the fit. Fitted gradients from the literature are also shown as the colored lines indicated in the legends. Top panel: the oxygen abundance gradient. In the legend, the first citation is the study, while the second citation abbreviated in parentheses is the calibration method used: P05 (L. S. Pilyugin 2005), KK04 (H. A. Kobulnicky & L. J. Kewley 2004), PT05 (L. S. Pilyugin & T. X. Thuan 2005), PG16 (L. S. Pilyugin & E. K. Grebel 2016). Middle panel: the $\log \mathcal{U}$ radial gradient. Bottom panel: the N/O radial gradient. Those H II regions with only lower limits are shown as faint upward arrows. These are not included in the fit.

harder prior on the oxygen abundances, namely $\mathcal{N}(9, 0.1)$, making direct comparisons to SIGNALS difficult.

Figure 8 shows the recovered radial gradients for three parameters: oxygen abundance (top panel), ionization parameter (middle panel), and N/O ratio (bottom panel). In order to

fit a radial gradient, we take the median in bins with a width of $0.1R_{25}$. We derive uncertainties on the bins using a Monte Carlo algorithm, which randomly samples each data point within its uncertainties 1000 times. The uncertainty on the bin is then the standard deviation of these samples. The gradient is then fit to the binned data. Table 2 reports the resulting fits, the scatter in the raw and binned data, and the Spearman correlation coefficients for both the raw and binned data. In what follows, we compare our gradients with those from the literature, noting differences and similarities.

Starting with the oxygen abundance gradient in the top panel of Figure 8, we see that our fitted gradient closely matches the slope of that reported by J. Moustakas et al. (2010) using the theoretical R_{23} calibration of H. A. Kobulnicky & L. J. Kewley (2004; solid blue line). This agreement is not surprising, as we have given NebulaBayes the R_{23} ratio as a prior. Our gradients are the same within the uncertainties with the J. Moustakas et al. (2010) gradient shifted upward by ~ 0.2 dex. We have a steeper gradient than those estimated by electron temperature measurements (F. F. Rosales-Ortega et al. 2011; D. A. Berg et al. 2020; red dashed and solid lines, respectively) with ours shifted upward by ~ 0.3 dex. Similarly, the gradient reported by J. Moustakas et al. (2010) using the empirical P -method of L. S. Pilyugin & T. X. Thuan (2005; dashed blue line) shows a much lower and shallower gradient, shifted downward from the T_e gradients by a further ~ 0.3 dex. These are known issues in comparing abundances derived with different calibrations, and we refer the reader to the discussion of J. Moustakas et al. (2010). Despite these concerns, the fact that the abundances estimated through NebulaBayes broadly agree with those from more established methods is comforting.

Turning to the ionization parameter gradient in the middle panel of Figure 8, we recover a weak positive gradient. We note that it is not the two binned points beyond $1.3R_{25}$ that is determining the positive gradient; rather, it is being determined by the points between $0.3R_{25}$ and $0.9R_{25}$. Most galaxies show a shallow or flat gradient in $\log \mathcal{U}$. However, F. F. Rosales-Ortega et al. (2011) noted an increase with radius beyond $0.3R_{25}$ for the entire galaxy, a trend more evident when they split the galaxy into quadrants. Figure 8 shows their fitted gradients for the north and south quadrants, red dashed and dashed-dotted lines, respectively, which contain the largest and brightest H II regions in the galaxy and are the most populated by number in their study. The positive gradients seen here could represent any number of changing physical conditions with radius (see F. F. Rosales-Ortega et al. 2011 for a discussion).

Finally, in the bottom panel of Figure 8, we show the N/O radial gradient. Notably, we recover a similar gradient within the uncertainties to those derived with T_e abundances (F. F. Rosales-Ortega et al. 2011; D. A. Berg et al. 2013, 2020). These studies also demonstrated that a piecewise function best describes the N/O gradient, with the N/O ratio flattening at approximately the R_{25} . We did not fit a piecewise function to our data due to the paucity of data points beyond R_{25} , but the N/O ratio appears to plateau at a value of -1.37 ± 0.08 . The appearance of this plateau could be an effect of a combination of the primary and secondary nitrogen production in the outermost H II regions (M. Mollá et al. 2006).

Despite the difficult choice of priors, useful line fluxes, and error weighting, we have recovered the known gradients in O/H, $\log \mathcal{U}$, and N/O for NGC 628. While we infer a steeper O/H gradient than those determined by T_e measurements

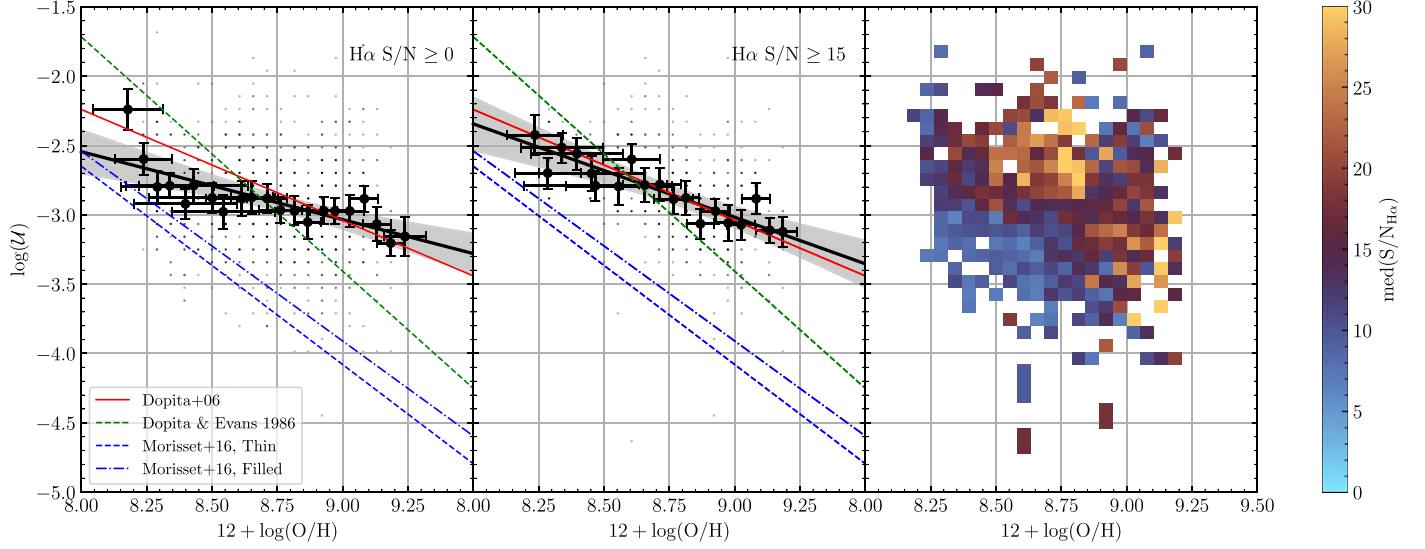


Figure 9. The $\log \mathcal{U}$ - O/H relation. Left panel: all H II regions. Middle panel: only H II regions with $\text{H}\alpha \text{ S/N} \geq 15$. Individual H II regions are shown as small points that are binned in O/H with a bin width of 0.05 dex. Uncertainties are estimated using a Monte Carlo algorithm. The black line is the fit to the binned data. Relations from the literature are also plotted: M. A. Dopita et al. (2006) in red, M. A. Dopita & I. N. Evans (1986) in dashed green, and the thin shell model (dashed blue) and filled sphere model (dashed-dotted blue) from M16. Fits are given in Table 2. Right panel: 2D histogram of the median $\text{H}\alpha \text{ S/N}$ in each bin.

(F. F. Rosales-Ortega et al. 2011; D. A. Berg et al. 2013, 2020), our gradient is consistent with other strong-line methods that use the same emission lines that we have (J. Moustakas et al. 2010). The $\log \mathcal{U}$ and N/O gradients agree more readily with other spectroscopic data, even recovering a possible plateau in N/O at large radii. This remarkable ability for NebulaBayes to estimate the physical properties of H II regions in NGC 628 gives confidence in this method, allowing us to turn to correlations between these properties.

6. The $\log \mathcal{U}$ - O/H Correlation

Numerous studies have investigated the potential correlation between the ionization parameter and oxygen abundance. M. A. Dopita et al. (2006) predicted an anticorrelation of the form $\mathcal{U} \propto Z^{-0.8}$ based on a theoretical calculation of a wind-driven bubble model for H II regions. More recent studies using a large sample of H II regions or star-forming galaxies have since supported this theoretical expectation (C. Maier et al. 2006; T. Nagao et al. 2006; E. Pérez-Montero 2014; C. Morisset et al. 2016; A. D. Thomas et al. 2019). However, other studies have found there to be either no correlation or a positive correlation (e.g., O. L. Dors et al. 2011; M. A. Dopita et al. 2014; H. Poetrodjojo et al. 2018; K. Kreckel et al. 2019; M. Mingozzi et al. 2020; X. Ji & R. Yan 2022), in direct contrast to M. A. Dopita et al. (2006).

Figure 9 shows the relation between $\log \mathcal{U}$ and oxygen abundance for NGC 628 using SIGNALS data. In the left panel, we show all H II regions in our data set, while in the middle panel, we show only those with an $\text{H}\alpha \text{ S/N} \geq 15$, which consists of 47% of the total number of regions. The right panel displays a 2D histogram of the median S/N in each bin. Similarly to fitting the gradients in Section 5, we binned the data in both panels in equally spaced abundance bins of 0.05 dex estimating uncertainties in the bins using a Monte Carlo algorithm run 1000 times. Given the uncertainties in both the x - and y -directions, we fit these binned data points using `scipy.odr`, an implementation of orthogonal distance regression, weighting the fits on each axis by the standard

deviations within each bin. In the fit to all data, we find a relation of the form $\mathcal{U} \propto Z^{-0.50 \pm 0.09}$, while the fit to the high-S/N sample gives a relation of $\mathcal{U} \propto Z^{-0.67 \pm 0.08}$. Table 2 gives the full parameterization of our fits in both panels.

Additionally, we added the theoretical relations from M. A. Dopita & I. N. Evans (1986) and M. A. Dopita et al. (2006) as well as the relation of M16 derived from photoionization modeling. Since M. A. Dopita et al. (2006) only reported a proportionality, namely $\mathcal{U} \propto Z^{-0.8}$, in order to plot it, we fit this function to our binned data in each panel while fixing the slope to -0.8 . This fit is easily done in `scipy.odr` using the `ifixb` argument. In both cases, the resulting y -intercept is identical within the uncertainties.

We easily find a negative anticorrelation between $\log \mathcal{U}$ and O/H in agreement with the predictions of M. A. Dopita et al. (2006). Both sample selections show a statistically significant anticorrelation in the binned data (Table 2), with the higher-S/N sample matching that of M. A. Dopita et al. (2006) within the uncertainties. Note that we did not assume these two quantities would be anticorrelated in our CLOUDY models or NebulaBayes parameter estimation. The fact that we still find this anticorrelation suggests a physical connection between the two parameters.

This finding is in direct tension with those studies that did not find an anticorrelation for individual galaxies (D. R. Garnett et al. 1997; O. L. Dors et al. 2011; M. A. Dopita et al. 2014; H. Poetrodjojo et al. 2018; M. Mingozzi et al. 2020; K. Grasha et al. 2022). K19 proposes that those studies that do not find an anticorrelation are generally spatially resolved studies. However, we suggest that these are not truly spatially resolved, as they could not have resolved individual H II regions at their galaxies' distances. For instance, the best spatial resolution of these studies was that of M. A. Dopita et al. (2014) with an average spatial resolution of ~ 460 pc. Others had even higher spatial resolutions up to ~ 2 kpc (H. Poetrodjojo et al. 2018; M. Mingozzi et al. 2020). While H II regions do come in a wide variety of physical sizes, taking 100 pc as a reference value (M. Azimlu et al. 2011) means that many of these previous

studies could not have resolved individual H II regions and were likely blending multiple H II regions together.

Compare these resolutions to the SITELLE (seeing limited) angular resolution of 1'', which, at NGC 628, corresponds to a spatial resolution of 35 pc. Our smaller resolution allows us to measure the emission-line properties of small H II regions that simply cannot be measured by other studies while also allowing us to account for all of the emission from larger H II regions. However, K. Kreckel et al. (2019) used data for NGC 628 taken from the MUSE spectrograph, which has a similar spatial resolution to SITELLE, and they found a positive correlation between abundance and ionization parameter.¹⁴ It is worth mentioning how our two studies differ and how that might lead to our two contrary findings.

First, the spatial coverage of MUSE is limited to only the inner $0.5R_{25}$ of NGC 628. If we limit our data to only the inner $0.5R_{25}$ and plot the resulting $\log \mathcal{U}$ -O/H correlation, we recover a weak positive correlation with a slope of 0.11 ± 0.08 with a Spearman ρ coefficient of $+0.16$ at $p = 0.51$. NGC 628 was one of the galaxies in their sample for which this trend was weak; they measured a Spearman coefficient of $+0.19$ between oxygen abundance and S_{32} .

A few more considerations preclude a direct comparison between our samples. The spectral coverage of MUSE does not include the [O II] doublet. To estimate oxygen abundance, they used the S -calibration of L. S. Pilyugin & E. K. Grebel (2016), which utilizes the [N II], [S II], and [O III] emission lines and shows minor differences compared to auroral line estimates. The effect of this calibration is a shallow abundance gradient (Figure 8) with less dynamic range; they report abundances in the range of ~ 8.4 – 8.6 dex.

Furthermore, K. Kreckel et al. (2019) avoided the problems with various \mathcal{U} calibrations by only comparing oxygen abundance to S_{32} . However, they did not correct any of their emission-line measurements for the DIG, which should elevate the integrated [N II] and [S II] fluxes. Not making this correction has several compounding effects. When blended with the emission from an H II region, the DIG can: artificially flatten metallicity gradients (K. Zhang et al. 2017; H. Poetrodjojo et al. 2019), lead to a misclassification of regions in the BPT diagrams (E. Congiu et al. 2023), and lead to an underestimate of S_{32} (F. Belfiore et al. 2022). These all likely strongly affect the resulting $\log \mathcal{U}$ -O/H correlation that they measure. For instance, K. Kreckel et al. (2019) estimated that a DIG correction would increase by $\sim 70\%$ of their S_{32} ratios. Given our extensive spatial coverage, DIG corrections, and self-consistent estimates of oxygen abundance and ionization parameter, the anticorrelation found in Figure 9 is likely robust against comparing our two studies. A forthcoming paper will present a direct comparison of the MUSE H II regions and SIGNALS H II regions in NGC 628 (J. Vandersnickt et al. 2025, in preparation).

Despite the anticorrelation between $\log \mathcal{U}$ and O/H that we find in the binned data, there is still a significant scatter in the raw, unbinned data. In other words, at any fixed oxygen abundance, there is a large spread in $\log \mathcal{U}$ between 1 and 2.5 dex. This scatter implies that factors other than oxygen abundance drive the variation in $\log \mathcal{U}$ within the sample.

¹⁴ K. Kreckel et al. (2019) did not report any linear fits to the $\log \mathcal{U}$ -O/H correlation they found, only noting that the correlation is positive and reporting the correlation coefficient. See Figure 6 in K. Kreckel et al. (2019).

6.1. Internal Dust Extinction in H II Regions

We cannot ignore the impact of dust on the ionizing spectrum seen by the gas cloud. Dust will change the temperature structure of a cloud since it provides alternate heating and cooling mechanisms. However, an H II region must be cool enough to allow for the survival of dust grains, so any dust effects should only matter in high-abundance H II regions where cooling mechanisms dominate and dust can survive (B. T. Draine 2011). Meanwhile, the wavelength dependence of dust extinction will naturally lead to a softening of the ionizing spectrum. Dust extinction usually explains why \mathcal{U} generally does not get higher than approximately -2 (M. A. Dopita et al. 2002; S. C. C. Yeh & C. D. Matzner 2012). Therefore, we expect two trends: as dust extinction increases, oxygen abundance should increase while \mathcal{U} decreases.

Figure 10 shows the trend with dust extinction as measured by the color excess, $E(B - V)$, for both oxygen abundance and $\log \mathcal{U}$ separated by $H\alpha$ S/N in the left and right columns. In all cases, we binned the data in equally spaced bins of $E(B - V)$ with widths of 0.05 dex and used a Monte Carlo algorithm to estimate the uncertainties in the bins. We again used `scipy.odr` to fit these binned data points, weighting by the standard deviations in each bin. Table 2 gives the full parameterizations.

We see a shallow positive correlation between $E(B - V)$ and O/H with a slope of 0.11 ± 0.05 and a strong negative correlation between $E(B - V)$ and $\log \mathcal{U}$ with a slope of -0.61 ± 0.08 when fitting all H II regions. The shallow slope of the O/H- $E(B - V)$ relation is concerning, but this is likely an S/N effect. The right column of Figure 10 shows the fit for only H II regions with an $H\alpha$ S/N ≥ 15 where we recover a slightly stronger positive correlation between $E(B - V)$ and oxygen abundance with a slope of 0.19 ± 0.07 . Still, NGC 628 does have a relatively constant dust-to-gas ratio (L. Kahre et al. 2018; J. M. Vilchez et al. 2019), implying a relatively flat O/H- $E(B - V)$ relation. Meanwhile, the trend with $\log \mathcal{U}$ remains strongly negative regardless of the S/N bin with a slope of -0.65 ± 0.11 , indicating that dust strongly modifies the ionizing spectrum of an H II region.

As another way of looking at these trends, Figure 11's top two panels shows a 2D histogram of the $\log \mathcal{U}$ -O/H anticorrelation colored by median extinction in each bin. Both panels shows the anticorrelation, for the whole data set (top panel) as well as for high-S/N points, $S/N \geq 15$ (middle panel). We see that, especially for the high-S/N data, there is a trend in extinction along the anticorrelation. Namely, those H II regions with high oxygen abundances and low ionization parameters have generally high dust extinction and vice versa. Looking at all data points slightly washes out this trend, but it remains apparent.

Finally, if dust extinction is a significant driver of the anticorrelation between $\log \mathcal{U}$ and O/H, then we would expect that combining these properties into a “fundamental plane” would reduce the scatter compared to the simple 2D anticorrelation. The bottom panel of Figure 11 shows such a plane constructed using the `ltsfit` code (M. Cappellari et al. 2013). This robust method fits a linear function to n -dimensional data, accounting for uncertainties in all coordinates and intrinsic scatter. We linearly combine oxygen abundance and extinction against $\log \mathcal{U}$ for data points with $S/N \geq 15$. The coefficients for the fit are provided in the panel. We see that the scatter from Figure 9 has been reduced by about 0.1 dex by including dust extinction in the correlation.

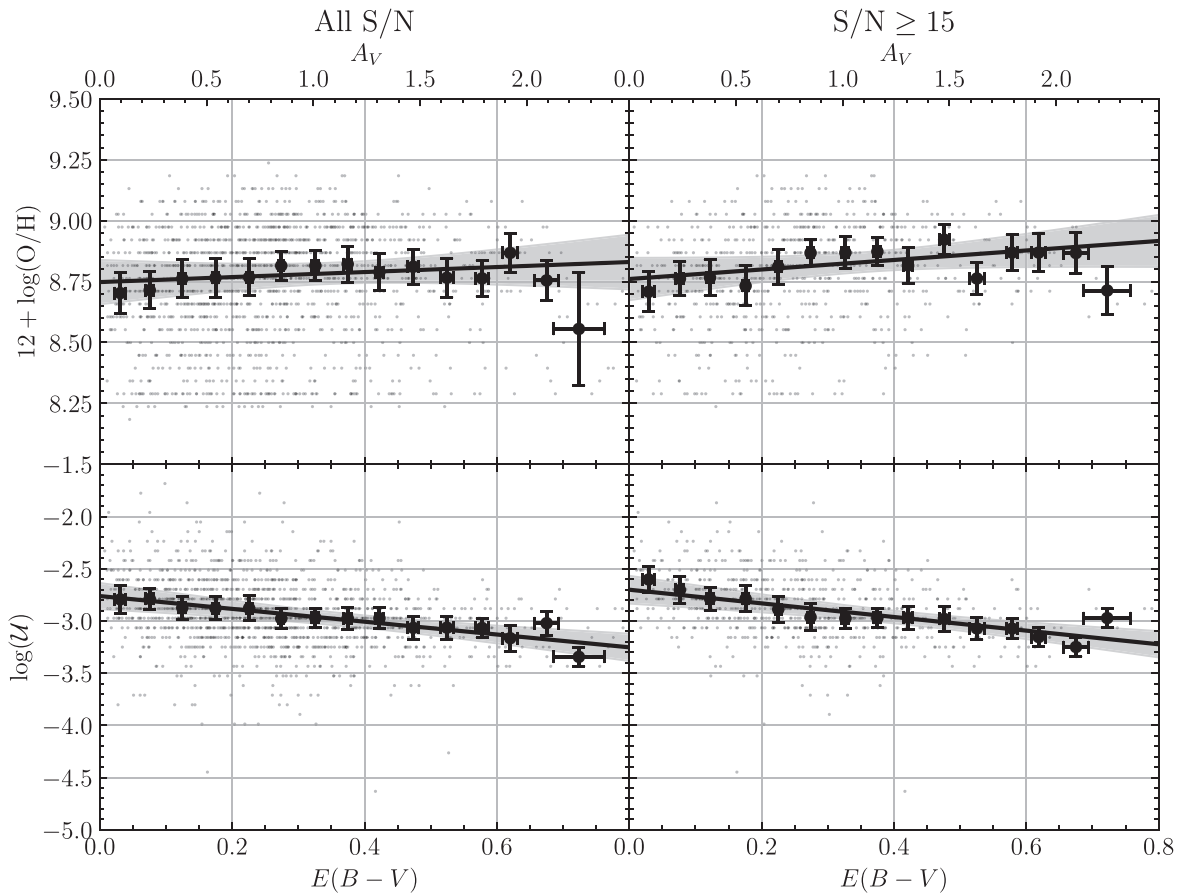


Figure 10. The relationship between O/H or $\log \mathcal{U}$ and dust extinction. The bottom x -axis is the color excess, $E(B - V)$, while the top x -axis shows extinction, A_V , assuming Milky Way reddening. Left column: all H II regions. Right column: only H II regions with $H\alpha$ S/N ≥ 15 . Individual H II regions are shown as small points that are binned in $E(B - V)$ with a bin width of 0.05. Uncertainties are estimated using a Monte Carlo algorithm. The black line is a fit to the binned data; parameterization is reported in Table 2.

This fit is also statistically significant with a Spearman coefficient of $\rho = +0.54$ at $p = 0$. Thus, dust might be key in understanding the scatter observed in the $\log \mathcal{U}$ -O/H anticorrelation.

An important question to answer is how sensitive our model results are to changes in the Balmer decrement used to derive $E(B - V)$. The Balmer decrement depends on the temperature (and thus the metallicity) and density of an H II region (D. E. Osterbrock & G. J. Ferland 2006). Using the range of electron temperatures found by CHAOS for NGC 628 and the range of densities we measure, we calculated the Balmer decrement given this grid of temperatures and densities using PyNeb, resulting in a minimum Balmer decrement of 2.79 at low abundances and a maximum of 3.04 at high abundances. We recalculated the dust extinction, abundances, and ionization parameters, assuming these new Balmer decrement extremes. We found that while the individual properties of any H II region might change, the overall bulk properties of the sample did not. In other words, we found the same trends with extinction and the same anticorrelation as we had before assuming a constant Balmer decrement of 2.86. Therefore, our conclusions are not sensitive to changes in the Balmer decrement.

All of this points toward the important consequences dust has on the observed ionizing spectrum of an H II region. For instance, several analytical and numerical models (e.g., V. Petrosian et al. 1972; L. Spitzer 1978; S. J. Arthur et al. 2004; T. J. Haworth et al. 2015; A. A. Ali 2021) predict that as

the dust opacity of an H II region increases, the size of the H II region should shrink. This is explained by dust absorbing ionizing photons, reducing the pressure gradient between the ionized and neutral gas, and shrinking the H II region compared to one with no dust (A. A. Ali 2021). Decreasing the size while holding all else constant would raise the ionization parameter according to Equation (1). Thus, we would expect the opposite of our $\log \mathcal{U}$ - $E(B - V)$ trends here. However, the ionization parameter defined at the Strömgren radius as in Equation (1) would be outside the H II region, so this might require a redefinition of the ionization parameter (X. Ji & R. Yan 2022). The impact of dust on the geometry of an H II region and what it means for the $\log \mathcal{U}$ -O/H anticorrelation is beyond the scope of this paper, as it requires sophisticated combinations of dynamical and photoionization models of dusty H II regions.

6.2. $H\alpha$ Surface Brightness

Star formation plays a vital role in regulating the chemical enrichment of a galaxy. It is well-known that a correlation exists between the global metallicity and stellar mass in star-forming galaxies, i.e., the mass–metallicity relation (J. Lequeux et al. 1979; C. A. Tremonti et al. 2004). There may also be an additional dependence on the SFR (e.g., M. A. Lara-López et al. 2010; F. Mannucci et al. 2010). Spatially resolved studies have shown that this relationship still holds on smaller scales

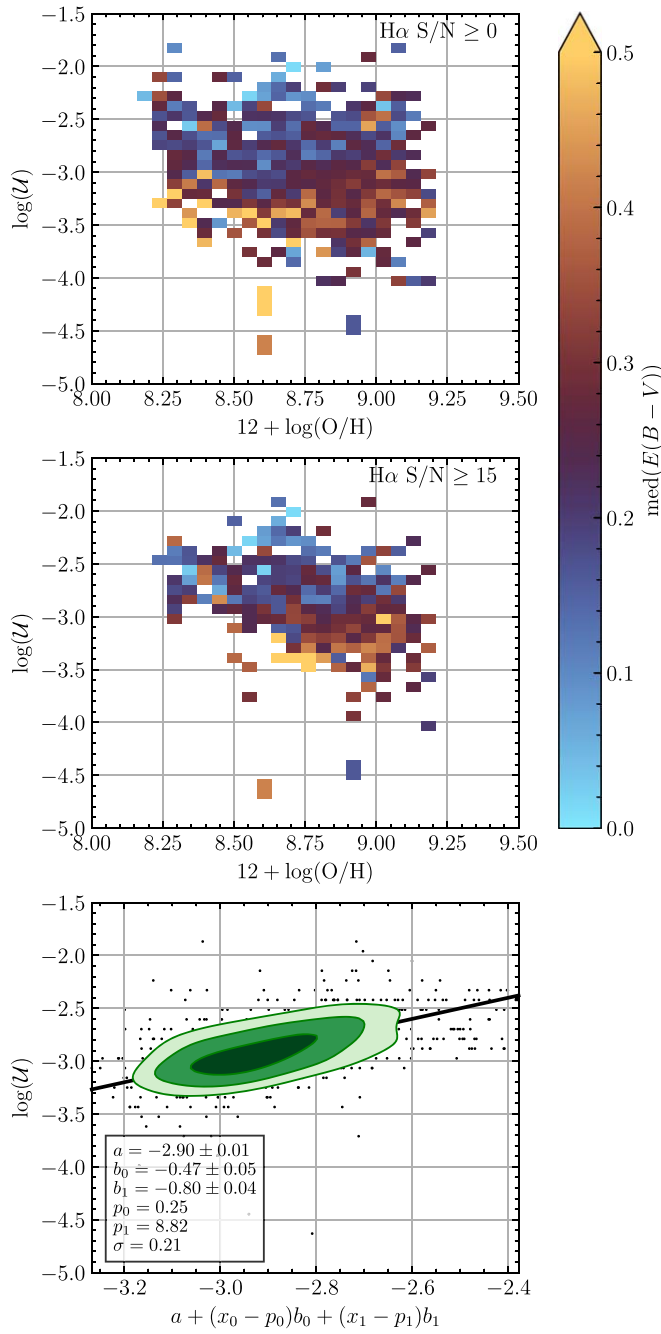


Figure 11. Top panel: the 2D histogram of the $\log \mathcal{U}$ –O/H anticorrelation with bins colored by dust extinction. This panel includes all points, regardless of $H\alpha$ S/N. Middle panel: same as the top panel except only for those regions with $H\alpha$ S/N ≥ 15 . Bottom panel: a “fundamental plane” combining dust extinction and oxygen abundance on the x-axis and $\log \mathcal{U}$ on the y-axis. Here, $x_0 = E(B-V)$ and $x_1 = 12 + \log(O/H)$. The green contours enclose 30%, 50%, and 80% of the data points.

for individual star-forming regions (F. F. Rosales-Ortega et al. 2012).

What is less clear is if the ionization parameter also depends on SFR. Some studies have reported a possible correlation between ionization and SFR. M. A. Dopita et al. (2014) found such a correlation for a set of 10 star-bursting luminous infrared galaxies, and other studies have found a similar correlation in the low- and high-redshift Universe (K. F. Kaplan et al. 2016; N. A. Reddy et al. 2023a, 2023b). One possible way to relate the ionization parameter to the SFR is through cluster mass, to

which M. A. Dopita et al. (2006) found \mathcal{U} is related. Following the derivation in X. Ji & R. Yan (2022), if \mathcal{U} is regulated through the SFR surface density via $\mathcal{U} \propto \Sigma_{\text{SFR}}^\alpha$ with the cluster mass being the medium, then $\alpha < 0.2$.

Figure 12 shows the spatially resolved $\Sigma_{H\alpha}$ correlations of O/H and $\log \mathcal{U}$ for our H II regions separated into two $H\alpha$ S/N samples, all H II regions (left column) and those with $H\alpha$ S/N ≥ 15 (right column). We used the extinction-corrected $\log \Sigma_{H\alpha}$ to represent $\log \Sigma_{\text{SFR}}$, as they differ only by a constant (C.-N. Hao et al. 2011; E. J. Murphy et al. 2011; R. C. Kennicutt & N. J. Evans 2012); although, we show the corresponding SFR surface density along the top axis. In all cases, we binned the data in equally spaced bins of 0.2 dex and again used a Monte Carlo algorithm to estimate the bin uncertainties. Bins with only one H II region appear as transparent circles in Figure 12, and the fitting algorithm does not include them. Table 2 provides the full parameterizations of the fits.

Regardless of the S/N sample, both relations show very shallow slopes that are consistent with being flat. While this means we do have $\alpha < 0.2$, given the lack of statistical significance, it is unlikely that the very weak O/H–SFR and $\log \mathcal{U}$ –SFR relations could give rise to the stronger $\log \mathcal{U}$ –O/H anticorrelation. Not finding a relationship between these two quantities is perhaps not unexpected since NGC 628 is not a starburst galaxy. Comparing our data to that of M. A. Dopita et al. (2014), while we do have H II regions with $\log \mathcal{U} \gtrsim -3.3$, we do not have extremely star-forming regions. Using their Figure 13 as a guide, we observe that their positive correlation starts at approximately $\log \Sigma_{\text{SFR}} \simeq -0.5$ or $\log \Sigma_{H\alpha} \simeq 40.5$. Only 31 H II regions have such high-ionization parameters and luminosity surface densities in our sample (colored red in Figure 12). Interestingly, if we fit only these 31 H II regions without binning, we recover a fit of the form $\mathcal{U} \propto \Sigma_{\text{SFR}}^{0.32 \pm 0.24}$, very similar to M. A. Dopita et al. (2014), who found an exponent of 0.34 ± 0.08 . This agreement is encouraging, but our lack of data points at these extreme conditions prevents us from making any robust conclusions about the role of luminosity surface density as a mediator of the main anticorrelation.

7. Conclusions

In this work, we have analyzed the properties over 1500 H II regions in the well-known, nearly face-on spiral galaxy NGC 628. The data were acquired using the CFHT spectro-imager SITELLE, which provides a spatial resolution of ~ 35 pc and a spectral resolution ranging from $R \sim 600$ in the blue (~ 3745 Å) up to $R \sim 1800$ in the red (~ 6670 Å). The instrument’s sensitivity enabled us to detect very faint H II regions, down to $38.5 \text{ erg s}^{-1} \text{ kpc}^{-2}$. Its extensive FOV, covering 11 arcmin^2 , encompassed the entire optical disk, including contributions from the diffuse ionized gas. This comprehensive coverage allowed us to investigate the potential correlation between the gas-phase oxygen abundance and the ionization parameter.

Just as is the case when estimating oxygen abundances, several calibrations for the ionization parameter exist in the literature. Unfortunately, as we have shown, these ionization parameter calibrations have the same issues as the oxygen abundance calibrations: differing atomic data sets, stellar SEDs, and chemical abundance sets that result in offsets of 0.5 dex or more. We strongly advise against blindly using these published calibrations without understanding their inherent assumptions and resulting uncertainties.

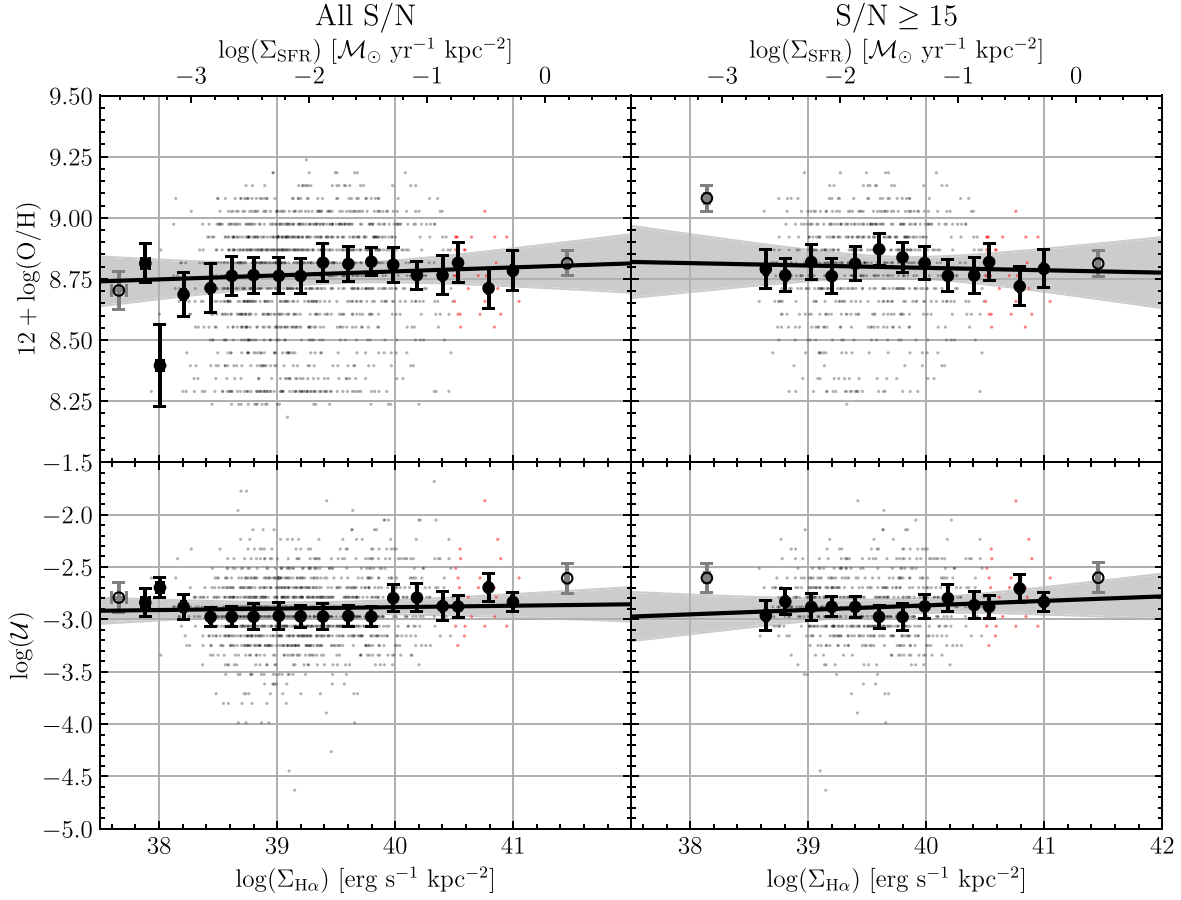


Figure 12. The O/H-log $\Sigma_{\text{H}\alpha}$ and log \mathcal{U} -log $\Sigma_{\text{H}\alpha}$ relations. The bottom x -axis is $\text{H}\alpha$ surface density while the top x -axis is the SFR surface density. Left column: all H II regions. Right column: only H II regions with $\text{H}\alpha$ S/N ≥ 15 . Individual H II regions are shown as small points that are binned in $\log \Sigma_{\text{H}\alpha}$ with a bin width of 0.2 dex. Those regions that satisfy the conditions explored in M. A. Dopita et al. (2014) are colored red; these are still included in the bins. Large black points with error bars are fitted, while those bins containing only one H II region are shown as transparent points and are not included in the fit. Uncertainties are estimated using a Monte Carlo algorithm. The black line is a fit to the solid binned data; the parameterization is reported in Table 2.

These issues motivated us to create our own custom photoionization models using the latest version of CLOUDY (M. Chatzikos et al. 2023). This allowed us to match the input parameters of the models as best as possible to the observed properties of our H II regions. We used the Bayesian inference code NebulaBayes (A. D. Thomas et al. 2018) to subsequently match those models to our H II regions to derive oxygen abundances, nitrogen abundances, and ionization parameters for each individual H II region. Our ability to reproduce the well-known gradients in NGC 628, consistent with those previously found in the literature (e.g., F. F. Rosales-Ortega et al. 2011; D. A. Berg et al. 2020), gives us confidence in the robustness of our methodology.

With our estimated physical parameters, we found an anticorrelation between the oxygen abundance and ionization parameter consistent with the theoretical predictions of a wind-driven bubble model for an H II region (M. A. Dopita et al. 2006). Namely, we recover an anticorrelation of the form $\mathcal{U} \propto Z^{-0.67 \pm 0.08}$ in those regions with high S/N. We claim that our results, which stand in tension with other studies, are found because we are able to resolve emission from H II regions from a wide variety of physical scales due to our small angular resolution, $\sim 1''$. K. Kreckel et al. (2019) used data taken from the MUSE spectrograph, which shares the same spatial resolution as SIGNALS at NGC 628, and found a positive correlation. While there are some differences in our data—

FOV, H II region extraction, and DIG correction—these variations present an exciting opportunity for further exploration of our findings. Work comparing our two catalogs is ongoing (J. Vandersnickt et al. 2025, in preparation).

However, there is still a high degree of scatter in this relationship. Searching for a secondary variable that could be the cause, we investigated potential trends with the dust extinction as measured through the color excess, $E(B-V)$, and the SFR surface density. We found strong trends with dust extinction in both ionization parameter and oxygen abundance: as the oxygen abundance increases and the ionization parameter decreases, the dust extinction increases on average. This is likely due to the well-known connection between dust and metallicity (e.g., B. T. Draine 2011) where only metal-rich H II regions are cool enough for dust to survive, and that dust absorbs ionizing photons, which reduces the ionization parameter. Incorporating dust extinction into a “fundamental plane” analysis of the O/H-log \mathcal{U} correlation reduces scatter by about 0.1 dex and shows a significant correlation, highlighting dust’s importance in understanding the anticorrelation. Meanwhile, we found no trends between either physical property with the SFR surface density. This is perhaps not expected, since NGC 628 is not a starburst galaxy in which this trend has been found in the past (M. A. Dopita et al. 2014).

As a concluding remark, we note that this research is only a first step. The nature of the correlation between oxygen

abundance and ionization parameter is still an open question, one which we hopefully have provided more insight to. As the SIGNALS team collects and reduces more data, we will add to the sample studied here, improving our ability to make statistical statements about multiple galaxies rather than only one.

Acknowledgments

The authors would like to thank the referee for providing helpful comments that improved the readability of the paper. R. G. would like to thank Justin Spilker for interesting and helpful discussions. This paper is based on data obtained for SIGNALS, a large program conducted at the Canada–France–Hawaii Telescope (CFHT), which is operated by the National Research Council of Canada, the Institut National des Sciences de l’Univers of the Centre National de la Recherche Scientifique of France, and the University of Hawaii. The observations were objected with SITELLE, a joint project of Université Laval, ABB, Université de Montréal and the CFHT, with support from the Canada Foundation for Innovation, the National Sciences and Engineering Research Council of Canada (NSERC), and the Fonds de Recherche du Québec—Nature et Technologies (FRQNT). The authors wish to recognize and acknowledge the very significant cultural role that the summit of Maunakea has always had within the indigenous Hawaiian community. We are most grateful to have the opportunity to conduct observations from this mountain.

Facility: CFHT.

Software: Astropy (Astropy Collaboration et al. 2013, 2018, 2022), Matplotlib (J. D. Hunter 2007), NumPy (C. R. Harris et al. 2020), SciPy (P. Virtanen et al. 2020), delta_method,¹⁵ NebulaBayes (A. D. Thomas et al. 2018), CLOUDY (M. Chatzikos et al. 2023), ltsfit (M. Cappellari et al. 2013), cmcrameri (F. Crameri 2018).

ORCID iDs

Ray Garner, III <https://orcid.org/0000-0002-9426-7456>
 Grace M. Olivier <https://orcid.org/0000-0002-4606-4240>
 David Fernández-Arenas <https://orcid.org/0000-0002-6874-4570>

References

- Ali, A. A. 2021, *MNRAS*, 501, 4136
 Ali, B., Blum, R. D., Bumgardner, T. E., et al. 1991, *PASP*, 103, 1182
 Allende Prieto, C., Lambert, D. L., & Asplund, M. 2001, *ApJL*, 556, L63
 Aller, L. H. 1942, *ApJ*, 95, 52
 Arthur, S. J., Kurtz, S. E., Franco, J., & Albarán, M. Y. 2004, *ApJ*, 608, 282
 Asplund, M., Grevesse, N., Sauval, A. J., & Scott, P. 2009, *ARA&A*, 47, 481
 Astropy Collaboration, Price-Whelan, A. M., Lim, P. L., et al. 2022, *ApJ*, 935, 167
 Astropy Collaboration, Price-Whelan, A. M., Sipőcz, B. M., et al. 2018, *AJ*, 156, 123
 Astropy Collaboration, Robitaille, T. P., Tollerud, E. J., et al. 2013, *A&A*, 558, A33
 Azimlu, M., Marciniak, R., & Barmby, P. 2011, *AJ*, 142, 139
 Badnell, N. R., Ferland, G. J., Gorczyca, T. W., Nikolić, D., & Wagle, G. A. 2015, *ApJ*, 804, 100
 Baldwin, J. A., Phillips, M. M., & Terlevich, R. 1981, *PASP*, 93, 5
 Belfiore, F., Santoro, F., Groves, B., et al. 2022, *A&A*, 659, A26
 Berg, D. A., Pogge, R. W., Skillman, E. D., et al. 2020, *ApJ*, 893, 96
 Berg, D. A., Skillman, E. D., Croxall, K. V., et al. 2015, *ApJ*, 806, 16
 Berg, D. A., Skillman, E. D., Garnett, D. R., et al. 2013, *ApJ*, 775, 128
- Blanc, G. A., Kewley, L. J., Vogt, F. P. A., & Dopita, M. A. 2015, *ApJ*, 798, 99
 Borsenberger, J., & Stasińska, G. 1982, *A&A*, 106, 158
 Bresolin, F., Kennicutt, R. C., & Garnett, D. R. 1999, *ApJ*, 510, 104
 Cantiello, M., Yoon, S.-C., Langer, N., & Livio, M. 2007, *A&A*, 465, L29
 Cappellari, M., Scott, N., Alatalo, K., et al. 2013, *MNRAS*, 432, 1709
 Cardelli, J. A., Clayton, G. C., & Mathis, J. S. 1989, *ApJ*, 345, 245
 Cedres, B., Beckman, J. E., Bongiovanni, A., et al. 2013, *ApJL*, 765, L24
 Chatzikos, M., Bianchi, S., Camiloni, F., et al. 2023, *RMaAA*, 59, 327
 Congiu, E., Blanc, G. A., Belfiore, F., et al. 2023, *A&A*, 672, A148
 Cowie, L. L., & Songaila, A. 1986, *ARA&A*, 24, 499
 Crameri, F. 2018, Scientific colour maps v4, Zenodo, doi:[10.5281/zenodo.2649252](https://doi.org/10.5281/zenodo.2649252)
 Croxall, K. V., Pogge, R. W., Berg, D. A., Skillman, E. D., & Moustakas, J. 2015, *ApJ*, 808, 42
 Croxall, K. V., Pogge, R. W., Berg, D. A., Skillman, E. D., & Moustakas, J. 2016, *ApJ*, 830, 4
 Dhungana, G., Kehoe, R., Vinko, J., et al. 2016, *ApJ*, 822, 6
 Díaz, A. I., Castellanos, M., Terlevich, E., & Luisa García-Vargas, M. 2000, *MNRAS*, 318, 462
 Díaz, A. I., Terlevich, E., Vilchez, J. M., Pagel, B. E. J., & Edmunds, M. G. 1991, *MNRAS*, 253, 245
 Díaz, A. I., & Zamora, S. 2022, *MNRAS*, 511, 4377
 Dinerstein, H. L., & Shields, G. A. 1986, *ApJ*, 311, 45
 Dopita, M. A., & Evans, I. N. 1986, *ApJ*, 307, 431
 Dopita, M. A., Fischer, J., Sutherland, R. S., et al. 2006, *ApJ*, 647, 244
 Dopita, M. A., Groves, B. A., Sutherland, R. S., Binette, L., & Cecil, G. 2002, *ApJ*, 572, 753
 Dopita, M. A., Rich, J., Vogt, F. P. A., et al. 2014, *Ap&SS*, 350, 741
 Dopita, M. A., Sutherland, R. S., Nicholls, D. C., Kewley, L. J., & Vogt, F. P. A. 2013, *ApJS*, 208, 10
 Dors, O. L., Krabbe, A., Hägele, G. F., & Pérez-Montero, E. 2011, *MNRAS*, 415, 3616
 Dors, O. L., Pérez-Montero, E., Hägele, G. F., Cardaci, M. V., & Krabbe, A. C. 2016, *MNRAS*, 456, 4407
 Draine, B. T. 2011, Physics of the Interstellar and Intergalactic Medium (Princeton, NJ: Princeton Univ. Press)
 Drissen, L., Martin, T., Rousseau-Nepton, L., et al. 2019, *MNRAS*, 485, 3930
 Eldridge, J. J., Langer, N., & Tout, C. A. 2011, *MNRAS*, 414, 3501
 Espinosa-Ponce, C., Sánchez, S. F., Morisset, C., et al. 2022, *MNRAS*, 512, 3436
 Evans, I. N. 1991, *ApJS*, 76, 985
 Ferguson, A. M. N., Gallagher, J. S., & Wyse, R. F. G. 1998, *AJ*, 116, 673
 Ferland, G. J. 1989, The Ohio State University Internal Report (Columbus, OH: Ohio State Univ.), 74
 Ferland, G. J., Korista, K. T., Verner, D. A., et al. 1998, *PASP*, 110, 761
 Ferland, G. J., Porter, R. L., van Hoof, P. A. M., et al. 2013, *RMaAA*, 49, 137
 Garnett, D. R. 1989, *ApJ*, 345, 282
 Garnett, D. R., Dufour, R. J., Peimbert, M., et al. 1995, *ApJL*, 449, L77
 Garnett, D. R., Shields, G. A., Skillman, E. D., Sagan, S. P., & Dufour, R. J. 1997, *ApJ*, 489, 63
 Goswami, S., Vilchez, J. M., Pérez-Díaz, B., et al. 2024, *A&A*, 685, A81
 Grasha, K., Chen, Q. H., Battisti, A. J., et al. 2022, *ApJ*, 929, 118
 Grevesse, N., Asplund, M., Sauval, A. J., & Scott, P. 2010, *Ap&SS*, 328, 179
 Hao, C.-N., Kennicutt, R. C., Johnson, B. D., et al. 2011, *ApJ*, 741, 124
 Harris, C. R., Millman, K. J., van der Walt, S. J., et al. 2020, *Natur*, 585, 357
 Haworth, T. J., Harries, T. J., Acreman, D. M., & Bisbas, T. G. 2015, *MNRAS*, 453, 2277
 Hillier, D. J., & Miller, D. L. 1998, *ApJ*, 496, 407
 Hunter, J. D. 2007, *CSE*, 9, 90
 Izotov, Y. I., Stasińska, G., Meynet, G., Guseva, N. G., & Thuan, T. X. 2006, *A&A*, 448, 955
 Izotov, Y. I., Thuan, T. X., & Wilson, J. C. 2009, *ApJ*, 703, 1984
 Jenkins, E. B. 1987, in Interstellar Processes, ed. D. J. Hollenbach & H. A. Thronson (Berlin: Springer), 533
 Jenkins, E. B. 2009, *ApJ*, 700, 1299
 Ji, X., & Yan, R. 2022, *A&A*, 659, A112
 Kahre, L., Walterbos, R. A., Kim, H., et al. 2018, *ApJ*, 855, 133
 Kaplan, K. F., Jogee, S., Kewley, L., et al. 2016, *MNRAS*, 462, 1642
 Kauffmann, G., Heckman, T. M., Tremonti, C., et al. 2003, *MNRAS*, 346, 1055
 Kennicutt, R. C. 1984, *ApJ*, 287, 116
 Kennicutt, R. C., & Evans, N. J. 2012, *ARA&A*, 50, 531
 Kennicutt, R. C., & Garnett, D. R. 1996, *ApJ*, 456, 504
 Kewley, L. J., & Dopita, M. A. 2002, *ApJS*, 142, 35

¹⁵ https://github.com/gjpellietter/delta_method/tree/main

- Kewley, L. J., Dopita, M. A., Sutherland, R. S., Heisler, C. A., & Trevena, J. 2001, *ApJ*, **556**, 121
- Kewley, L. J., & Ellison, S. L. 2008, *ApJ*, **681**, 1183
- Kewley, L. J., Groves, B., Kauffmann, G., & Heckman, T. 2006, *MNRAS*, **372**, 961
- Kewley, L. J., Nicholls, D. C., & Sutherland, R. S. 2019, *ARA&A*, **57**, 511
- Kobulnicky, H. A., & Kewley, L. J. 2004, *ApJ*, **617**, 240
- Kreckel, K., Ho, I.-T., Blanc, G. A., et al. 2019, *ApJ*, **887**, 80
- Kroupa, P. 2001, *MNRAS*, **322**, 231
- Lara-López, M. A., Cepa, J., Bongiovanni, A., et al. 2010, *A&A*, **521**, L53
- Leitherer, C., Ekström, S., Meynet, G., et al. 2014, *ApJS*, **212**, 14
- Leitherer, C., Ortiz Otálvaro, P. A., Bresolin, F., et al. 2010, *ApJS*, **189**, 309
- Lequeux, J., Peimbert, M., Rayo, J. F., Serrano, A., & Torres-Peimbert, S. 1979, *A&A*, **80**, 155
- Levesque, E. M., Kewley, L. J., & Larson, K. L. 2010, *AJ*, **139**, 712
- Li, S.-L., Grasha, K., Krumholz, M. R., et al. 2024, *MNRAS*, **529**, 4993
- Lin, L. I.-K. 1989, *Biome*, **45**, 255
- Luridiana, V., Morisset, C., & Shaw, R. A. 2015, *A&A*, **573**, A42
- Maier, C., Lilly, S. J., Carollo, C. M., et al. 2006, *ApJ*, **639**, 858
- Maiolino, R., & Mannucci, F. 2019, *A&ARv*, **27**, 3
- Mannucci, F., Belfiore, F., Curti, M., et al. 2021, *MNRAS*, **508**, 1582
- Mannucci, F., Cresci, G., Maiolino, R., Marconi, A., & Gnerucci, A. 2010, *MNRAS*, **408**, 2115
- Martin, T., Drissen, L., & Joncas, G. 2015, in ASP Conf. Ser. 495, Astronomical Data Analysis Software and Systems XXIV, ed. A. R. Taylor & E. Rosolowsky (San Francisco, CA: ASP), 327
- Martin, T. B., Prunet, S., & Drissen, L. 2016, *MNRAS*, **463**, 4223
- Martín-Navarro, I., Vazdekis, A., La Barbera, F., et al. 2015, *ApJL*, **806**, L31
- McCall, M. L., Rybski, P. M., & Shields, G. A. 1985, *ApJS*, **57**, 1
- Meynet, G., Maeder, A., Schaller, G., Schaerer, D., & Charbonnel, C. 1994, *A&AS*, **103**, 97
- Mihalas, D. 1972, Non-LTE Model Atmospheres for B and O Stars (Boulder, CO: National Center for Atmospheric Research)
- Mingozzi, M., Belfiore, F., Cresci, G., et al. 2020, *A&A*, **636**, A42
- Mollá, M., García-Vargas, M. L., & Bressan, A. 2009, *MNRAS*, **398**, 451
- Mollá, M., Vilchez, J. M., Gavilán, M., & Díaz, A. I. 2006, *MNRAS*, **372**, 1069
- Morisset, C., Delgado-Ingla, G., Sánchez, S. F., et al. 2016, *A&A*, **594**, A37
- Moustakas, J., Kennicutt, R. C., Tremonti, C. A., et al. 2010, *ApJS*, **190**, 233
- Murphy, E. J., Condon, J. J., Schinnerer, E., et al. 2011, *ApJ*, **737**, 67
- Nagao, T., Maiolino, R., & Marconi, A. 2006, *A&A*, **459**, 85
- Nicholls, D. C., Sutherland, R. S., Dopita, M. A., Kewley, L. J., & Groves, B. A. 2017, *MNRAS*, **466**, 4403
- Osterbrock, D. E., & Ferland, G. J. 2006, Astrophysics of Gaseous Nebulae and Active Galactic Nuclei (2nd ed.; Sausalito, CA: Univ. Science Books)
- Pagel, B. E. J., Edmunds, M. G., Blackwell, D. E., Chun, M. S., & Smith, G. 1979, *MNRAS*, **189**, 95
- Pauldrach, A. W. A., Hoffmann, T. L., & Lennon, M. 2001, *A&A*, **375**, 161
- Peimbert, M., Peimbert, A., & Delgado-Ingla, G. 2017, *PASP*, **129**, 082001
- Pellegrini, E. W., Rahner, D., Reissl, S., et al. 2020, *MNRAS*, **496**, 339
- Peluso, G., Radovich, M., Moretti, A., et al. 2023, *ApJ*, **958**, 147
- Pérez-Díaz, B., Masegosa, J., Márquez, I., & Pérez-Montero, E. 2021, *MNRAS*, **505**, 4289
- Pérez-Montero, E. 2014, *MNRAS*, **441**, 2663
- Pérez-Montero, E. 2017, *PASP*, **129**, 043001
- Petrosian, V., Silk, J., & Field, G. B. 1972, *ApJL*, **177**, L69
- Pilyugin, L. S. 2005, *A&A*, **436**, L1
- Pilyugin, L. S., & Grebel, E. K. 2016, *MNRAS*, **457**, 3678
- Pilyugin, L. S., & Thuan, T. X. 2005, *ApJ*, **631**, 231
- Poetrodjojo, H., D'Agostino, J. J., Groves, B., et al. 2019, *MNRAS*, **487**, 79
- Poetrodjojo, H., Groves, B., Kewley, L. J., et al. 2018, *MNRAS*, **479**, 5235
- Polimera, M. S., Kannappan, S. J., Richardson, C. T., et al. 2022, *ApJ*, **931**, 44
- Radovich, M., Poggianti, B., Jaffé, Y. L., et al. 2019, *MNRAS*, **486**, 486
- Reddy, N. A., Sanders, R. L., Shapley, A. E., et al. 2023a, *ApJ*, **951**, 56
- Reddy, N. A., Topping, M. W., Sanders, R. L., Shapley, A. E., & Brammer, G. 2023b, *ApJ*, **952**, 167
- Rosales-Ortega, F. F., Díaz, A. I., Kennicutt, R. C., & Sánchez, S. F. 2011, *MNRAS*, **415**, 2439
- Rosales-Ortega, F. F., Sánchez, S. F., Iglesias-Páramo, J., et al. 2012, *ApJL*, **756**, L31
- Rousseau-Nepton, L., Martin, R. P., Robert, C., et al. 2019, *MNRAS*, **489**, 5530
- Rousseau-Nepton, L., Robert, C., Martin, R. P., Drissen, L., & Martin, T. 2018, *MNRAS*, **477**, 4152
- Sánchez, S. F., Pérez, E., Rosales-Ortega, F. F., et al. 2015, *A&A*, **574**, A47
- Sánchez, S. F., Rosales-Ortega, F. F., Kennicutt, R. C., et al. 2011, *MNRAS*, **410**, 313
- Scheuermann, F., Kreckel, K., Barnes, A. T., et al. 2023, *MNRAS*, **522**, 2369
- Spearman, C. 1904, *Am. J. Psychol.*, **15**, 72
- Spitzer, L. 1978, Physical Processes in the Interstellar Medium (New York: Wiley)
- Stasińska, G. 1990, *A&AS*, **83**, 501
- Strom, A. L., Steidel, C. C., Rudie, G. C., Trainor, R. F., & Pettini, M. 2018, *ApJ*, **868**, 117
- Strömgren, B. 1939, *ApJ*, **89**, 526
- Sutherland, R., Dopita, M., Binette, R., & Groves, B., 2018 MAPPINGS V: Astrophysical Plasma Modeling Code, Astrophysics Source Code Library, ascl:1807.005
- Thomas, A. D., Dopita, M. A., Kewley, L. J., et al. 2018, *ApJ*, **856**, 89
- Thomas, A. D., Kewley, L. J., Dopita, M. A., et al. 2019, *ApJ*, **847**, 100
- Tremonti, C. A., Heckman, T. M., Kauffmann, G., et al. 2004, *ApJ*, **613**, 898
- Vale Asari, N., Stasińska, G., Morisset, C., & Cid Fernandes, R. 2016, *MNRAS*, **460**, 1739
- Veilleux, S., & Osterbrock, D. E. 1987, *ApJS*, **63**, 295
- Vila-Costas, M. B., & Edmunds, M. G. 1993, *MNRAS*, **265**, 199
- Vilchez, J. M., Relaño, M., Kennicutt, R., et al. 2019, *MNRAS*, **483**, 4968
- Vilchez, J. M., Pagel, B. E. J., Díaz, A. I., Terlevich, E., & Edmunds, M. G. 1988, *MNRAS*, **235**, 633
- Virtanen, P., Gommers, R., Oliphant, T. E., et al. 2020, *NatMe*, **17**, 261
- Xiao, L., Stanway, E. R., & Eldridge, J. J. 2018, *MNRAS*, **477**, 904
- Yeh, S. C. C., & Matzner, C. D. 2012, *ApJ*, **757**, 108
- Zhang, K., Yan, R., Bundy, K., et al. 2017, *MNRAS*, **466**, 3217
- Zou, H., Zhang, W., Yang, Y., et al. 2011, *AJ*, **142**, 16
- Zovaro, H. R. M., Sharp, R., Nesvadba, N. P. H., et al. 2020, *MNRAS*, **499**, 4940